A zebrafish circuit for behavioral credit assignment

Emanuele Paoli[1], Virginia Palieri[1,2], Amey Shenoy[1], Ruben Portugues[1,3,4,5]

[1] *Institute of Neuroscience, Technical University of Munich, Germany*
[2] *now at Champalimaud Center for the Unknown, Lisbon, Portugal*
[3] *SyNergy Excellence Cluster, Munich, Germany*
[4] *Bernstein Center for Computational Neuroscience, Munich, Germany*
[5] *Max Planck Fellow Group - Mechanisms of Cognition, MPI Psychiatry, Munich, Germany*

contact: ruben.portugues@tum.de
date: February 13, 2025

Abstract

An important question in systems neuroscience is how the brain links choices and their outcomes to modify future behavior. Despite being a fundamental computation, we lack explicit circuit-level models of how this is achieved. Here, we provide evidence for a cellular substrate underlying this computation in a vertebrate brain. We develop an operant thermoregulatory assay in larval zebrafish, and show that adaptive responses depend on the precise temporal coincidence between choices and contingent thermal feedback. Chemogenetic ablations reveal that the dorsal habenula (dHb), the homolog of the mammalian medial habenula, plays an essential role in this adaptive behavior. Functional and anatomical mapping of the downstream circuitry reveals that the intermediate interpeduncular nucleus (iIPN) integrates choice- and temperature-related signals, conveyed by the dHb and a prepontine hindbrain nucleus, respectively. While dHb axons exhibit a diffuse connectivity pattern, hindbrain neurons project onto specific, lateralized iIPN regions. We show that these iIPN glomeruli function as sensorimotor detectors, integrating choices and outcomes. Specifically, when a swim in a given direction is closely followed by a temperature change, iIPN activity shows increased responses. We further show that this coincidence detection, witha precise temporal profile, links an action to its subsequent sensory feedback, relies on a presynaptic mechanism within the terminal segments of dHb axons. This mechanism is mediated by $GABA_B$-dependent modulation of dHb sensory axons by choice-related prepontine GABAergic neurons. In this study we are therefore able to link an adaptive behavior to a specific circuit mechanism.

Introduction

A crucial step in most adaptive behaviors is determining which action lead to a certain outcome, a problem known as credit assignment [1]. This information can then be used to update the value of actions and adapt future behavior accordingly. While multiple circuits have been implicated in encoding different choice-outcome associations [2–6], it remains unclear where these representations first emerge and how they are mechanistically implemented.

To address this, we studied how zebrafish integrate behavioral choices and their sensory consequences, body temperature changes, to drive adaptive behavior. Using a thermoregulatory operant assay [7–13], we show that larval zebrafish adjust their reorientation behavior to minimize exposure to cold temperatures. This adaptation depends on the precise timing between a successful choice and its thermal feedback, as introducing a delay between the two impairs task performance. This suggests that coincidence detection between these sensorimotor events is a critical component of this adaptive process. Next, we focused on the dorsal habenula (dHb)–interpeduncular nucleus (IPN) pathway [14, 15], which is highly conserved across vertebrates, as chemogenetic ablation of the dHb specifically disrupted adaptive responses to aversive temperatures.

Through functional imaging of identified cell types we found that, while the right subnucleus of the dHb (r-dHb) signals sensory outcomes, neurons in the intermediate IPN (iIPN) report which choice caused that outcome, thus solving the credit assignment problem. We then performed electron microscopy (EM) reconstructions of this circuit and found that iIPN neurons, along with r-dHb

excitatory sensory inputs, receive behavioral choice signals from GABAergic neurons in the dorsal prepontine region (dPPR). Functional imaging and pharmacology experiments lead us to propose that choice-outcome coding is surprisingly mediated by presynaptic GABAb receptor (GABAbR) modulation of sensory axons. These results provide a circuit mechanism for integrating behavioral decisions with their consequences and could represent a canonical solution similarly implemented in other brain circuits.

Results

Operant thermoregulatory behavior in larval zebrafish

Larval zebrafish move in bouts that last $\sim$ 200 ms and that they elicit at a frequency of $\sim$ 1.25 Hz. To be able to deliver precisely timed stimuli with respect to these movements, we developed an assay in which fish could freely swim in a chamber with water at 20 °C. Their position was continuously monitored with a high-speed camera, and a set of galvanometric mirrors was used to direct an infrared laser directly to the larva's body (Figure S1a, see Methods)[16]. The laser was calibrated to increase the temperature locally by 1 °C to 21 °C (Figure S1b-d). Given that zebrafish prefer a temperature of $\sim$ 25.3 °C [17] a laser ON condition ($temp_{UP}$) is expected to have a positive valence for the larvae (Figure 1a).

We tested this hypothesis by defining a rectangular region (roi of interest, ROI) in the middle of the arena. Importantly, no positional cues indicated to the fish where this ROI was. When the fish entered this ROI, the laser was switched on, and when the fish left the ROI, the laser was switched off ($temp_{DOWN}$, Figure S1e). As expected, the larvae (n = 21 animals) consistently preferred the warmer region, compared to a control group (n = 5 animals) without IR heating (Figure S1f-h).

We previously reported that zebrafish larvae, when presented with aversive temperature changes, are able to flexibly turn clockwise (CW) or counterclockwise (CCW) depending on the animal's recent sensorimotor experience [17]. We built upon this phenomenon, and designed an operant thermoregulatory paradigm [7–13] that would allow us to isolate the minimal factors required to study how choices and sensory outcomes are integrated by the nervous system and used to guide behavior.

In this paradigm fish could increase their body temperature by turning in a specific direction (rule direction) and consequently minimize the time spent at a colder temperature. The experiment (n = 54 animals) consisted of 60 trials: 30 conditioned in one direction and 30 in the opposite direction, with the initial direction chosen randomly. Each trial (Figure 1b) began with a 10 second $temp_{UP}$ period during which an IR laser followed the fish. After this, and synchronized with any swim, the laser was turned off ($temp_{DOWN}$), initiating a cold period of up to 10 seconds. During the cold period, fish could quickly reactivate the laser (and therefore increase their body temperature, $temp_{UP}$) by turning in the rule direction. This would also lead to a 5 second inter-trial interval (ITI) where the laser is on before starting the next trial. If the fish did not turn in the rule direction within 10 seconds, the trial was aborted. To ensure that the fish had space to turn freely in both directions, trials were initiated only when the animal was distant from the arena borders (see Methods), resulting in a distribution of ITIs (Figure S2a).

We hypothesized that if zebrafish retain a memory of the previous trial's outcome and the associated choice that preceded it (choice-outcome event), their reorientation behavior after $temp_{DOWN}$ in the next trial should show a directional bias toward the rule direction. To test this hypothesis, we analyzed the angular velocity and the cumulative reorientation following $temp_{DOWN}$. The average angular velocity at $temp_{DOWN}$ matched the block's rule direction, with the fish reorienting toward the previously successful direction in increasing the body temperature (Figure 1c and Figure S2b-c). The same result was obtained by analyzing the cumulative reorientation of the first swim after $temp_{DOWN}$ (Figure 1d). This directional bias was not observed during the ITIs (Figure S2d-e), suggesting that the conditioned response is dependent on $temp_{DOWN}$. We next examined the influence that ITI has on the conditioned response. Interestingly, the bias was only observed during short ITIs (< 7.5 seconds) (Figure S2f), suggesting the involvement of a short-term memory from one trial to the next.

This behavior can be broken into three stages: (i) a turn (e.g. CW) leads to a positive outcome ($temp_{UP}$), which (ii) triggers a short-term memory process of the choice-outcome relationship, which subsequently (iii) is used to guide future responses at $temp_{DOWN}$ (repeating a CW turn, Figure S2g). For a sensory experience to be attributed as the result of a choice, the brain relies on a precise temporal relationship between the two. The choice must precede the sensory outcome, and the interval between them must be short. If a sensory event occurs without a preceding action, or after a significant delay, it is unlikely to be self-generated (i.e. to result from the animal's own movement). We therefore tested whether choice-outcome detection is impaired when a delay is imposed between the motor and sensory event (Figure 1e) by repeating the operant assay by applying a 0, 0.4 or 0.8 second delay (n = 20 animals for each condition).

Upon introducing a delay between the choice and the outcome, we observed a significant impairment in task performance when we analyzed the average cold exposure time corrected for delay (Figure 1f), reorientation bias (Figure 1g) and, surprisingly, the time elapsed between $temp_{DOWN}$ and fish response (reaction time, Figure S2h). Importantly, the innate temperature-induced turning behavior [17–19] per se was not affected by the perturbation, as evidenced when the absolute swim reorientation after $temp_{DOWN}$ was computed (Figure 2h). These results indicate that the sensorimotor delay impairs choice-outcome association (directional turning) but not the innate aversive-temperature responses (a-directional turning). The observed impairment highlights the importance of the precise temporal relationship between choice and outcome events. At the neuronal level, this phenomenon must be supported by a short-term memory process that is triggered by the choice-outcome detection.

The dorsal habenula is required for experience-dependent but not innate temperature responses

Previous studies have shown that the zebrafish dorsal habenula (dHb) is crucial for experience-dependent behaviors [20–23]. We previously reported that during thermal gradient navigation, dHb ablation impaired experience-dependent directional responses but not innate turning behavior [17].

We therefore tested whether the dHb is required for our operant assay, which, as described above, requires specific sensorimotor associations. We used a transgenic line to perform a chemogenetic ablation of dHb neurons (Figure 1i and Figure S2i, see Methods) and repeated the assay in ablated (n = 71 animals) and control groups (n = 72 animals, treatment control). The dHb ablation maintained the innate turning behavior intact (Figure 1j). However, we observed a significant decrease in the cold exposure time (Figure 1k), reorientation bias (Figure 1l) and a reaction time (Figure S2j), whereas other swimming parameters evaluated throughout the experiment were not affected (Figure S2k-n).

Overall, these findings indicate that the dHb is not directly involved in motor control or innate aversive sensorimotor responses. Instead, the contribution of the dHb is specific to regulating adaptive behaviors that require establishing a specific sensorimotor contingency, possibly for participating in the short-memory process or in the integration of choices and outcomes.

Functional imaging in the dHb - IPN pathway

Given the requirement of an intact dHb described above, we aimed to characterize neuronal responses associated with this behavior, starting with this region and its unique target, the interpeduncular nucleus (IPN) (Figure 2aI, Figure S3a-d). To investigate the relationship between choices, outcomes and neuronal activity, we implemented a head-fixed protocol with thermal conditions mimicking those used in our previous experiments (Figure 2aII, see Methods). In this protocol, temperature changes were temporally locked to the end of the animal's choices, which were detected online throughout the experiment [24, 25]. To facilitate statistical comparisons across conditions, the swim events triggered temperature changes randomly (Figure 3aIII left, see Methods). Specifically, each swim (regardless of amplitude or direction) had a probability of switching the current laser state from on to off or vice versa. As a result, swim decisions can be categorized by combinations of choices (CCW, CW or forward) and outcomes ($temp_{UP}$, $temp_{DOWN}$, or no change) (Figure 3aIII right). In addition to temperature changes, the fish experienced a continuous slow (3 mm/s) tail-to-head optic flow to ensure that they were motivated to swim throughout the entire duration of the experiment at a frequency of 0.28 ± 0.185 Hz. (mean ± st. dev.). Upon fish movements, we provided translational and rotational visual feedback, according to the animal's behavior.

We started by imaging neurons in the right subnucleus of the dHb (r-dHb, n = 14 animals), known to contain temperature-sensitive neurons [17, 18] (Figure S4aI). Indeed, we found both ON (fluorescence increases at $temp_{UP}$) and OFF responses (fluorescence increases at $temp_{DOWN}$, Figure S4aII-b). Using a shuffling procedure (see Methods), we found more ON than OFF neurons (Figure S4c). Analysis of ON neuron response dynamics (see Methods), revealed heterogeneous response profiles, which we categorized as fast-adapting (transient increase with rapid adaptation), fast non-adapting (sustained increase), and slow. Most neurons were slow or fast non-adapting (Figure S4d-e).

We then studied the activity in the target region of the dHb, the IPN. Based on neurons' somatic distribution, the IPN can be divided into a shell (or wall [26]), an elliptically shaped cluster of vGlut2a(+) neurons, and a core, a more spherical posterior vGlut2a(-) cluster enclosed by the shell (Figure S5a-b). Furthermore, IPN neurons extend their dendrites in neuropil regions called glomeruli, which are thought to constitute the computational unit of this region [24, 26]. We therefore used a transgenic line (Figure S5c) that, together with cerebellar eurydendroid cells [27], labels local glutamatergic IPN shell neurons [28] and their corresponding glomeruli (Figure S5d). We then imaged glomerular activity in the intermediate portion of the IPN (iIPN, Figure 2b, n = 19 animals), as is a region receiving r-dHb projections.

An intermediate IPN glomerulus functions as a sensorimotor coincidence detector

To our surprise, only one glomerulus per side showed elevated activity during our protocol (Figure 2b bottom right, blue and red arrows, from now on left- and right-$glomerulus^{iIPN}$). In stark contrast to what we observed in the r-dHb, this glomerular activity was variable, with clear transients at $temp_{UP}$ occurring only a fraction of the time. Closer inspection revealed a strong relationship between this variability and the animal's behavior. Specifically, when a reorientation swim triggered a $temp_{UP}$, calcium transients were observed only in the contralateral $glomerulus^{iIPN}$ relative to the turned direction. Figure 2c provides an example that depicts the activity of the left- (blue trace) and right-$glomerulus^{iIPN}$ (red trace). When the animal turns CCW or CW but this choice does not lead to a temperature change (no outcome), the glomeruli are almost silent. However, when the same type of movement leads to an increase in body temperature, the $glomerulus^{iIPN}$ located in the hemisphere contralateral to the turned direction strongly increases its fluorescence (Figure 2c right, Figure 2d, Figure S5e). Note that the change in temperature is triggered at movement termination and, considering the stochastic nature of our stimulation protocol, the animal cannot predict the outcome of each swim. Indeed, we did not find any difference in either tail directional bending or swim vigor when different action-outcome combinations were considered Figure S5f-g). Interestingly, once active, glomerular activity did not return to baseline like motor-modulated cells but instead remained active, resembling a sensory neuron (Figure 2c right).

Choice-outcome tuning was then analyzed on the basis of hemispheric glomerular positions. First, we calcu-

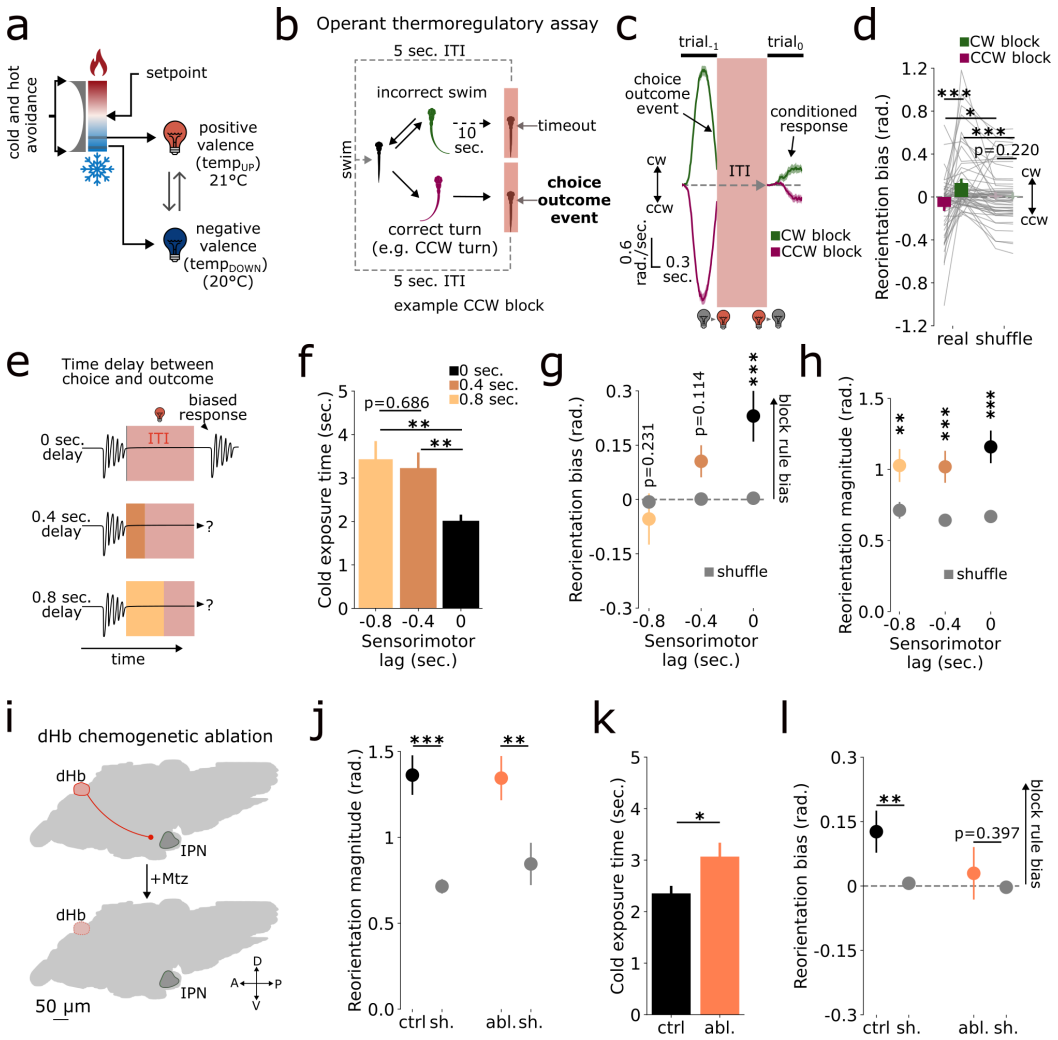

Figure 1: ***Operant thermoregulatory behavior in larval zebrafish (a)*** *Experimental concept. Thermoregulation is a symmetric process centered around the animal's setpoint. Deviations from this value trigger cold or hot avoidance behaviors. The laser modulates body temperature between two cold-aversive values, but when the laser is on the fish (temp$_{UP}$), the temperature remains closer to the setpoint compared to the temp$_{DOWN}$ condition.* ***(b)*** *Trial structure of the operant assay. Fish can increase body temperature by turning in the rule direction (either CCW or CW).* ***(c)*** *Angular velocity (mean ± s.e.m.) at choice-outcome events (end of preceding trial without timeout) and the start of the next trial, showing the conditioned response (magenta: CCW block, green: CW block).* ***(d)*** *First choice average reorientation (mean ± s.e.m.) at temp$_{DOWN}$ for CCW (magenta) and CW (green) blocks (first two bars) and their shuffles (third and fourth bars). Each line represents a single fish.* ***(e)*** *Concept of the choice-outcome delay experiment.* ***(f)*** *Cold exposure time corrected for delay condition (mean ± s.e.m.). Each bar represents the time between temp$_{DOWN}$ and the correct choice (black: 0 sec. delay, dark brown: 0.4 sec. delay, light brown: 0.8 sec. delay).* ***(g)*** *First choice average reorientation (mean ± s.e.m.) at temp$_{DOWN}$, with CCW and CW blocks pooled together (black: 0 sec. delay, dark brown: 0.4 sec. delay, light brown: 0.8 sec. delay, gray: shuffles).* ***(h)*** *First choice average reorientation magnitude (mean ± s.e.m.) at temp$_{DOWN}$, with CCW and CW blocks pooled together (black: 0 sec. delay, dark brown: 0.4 sec. delay, light brown: 0.8 sec. delay, gray: shuffles).* ***(i)*** *Schematic of dorsal habenula chemogenetic ablation experiment.* ***(j)*** *First choice average reorientation magnitude (mean ± s.e.m.) at temp$_{DOWN}$, with CCW and CW blocks pooled together (black: treatment control group, pink: ablation group, gray: shuffles).* ***(k)*** *Cold exposure time (mean ± s.e.m.). Each bar represents the time between temp$_{DOWN}$ and the correct choice (black: treatment control group, pink: ablation group, gray: shuffles).* ***(l)*** *First choice average reorientation (mean ± s.e.m.) at temp$_{DOWN}$, with CCW and CW blocks pooled together (black: treatment control group, pink: ablation group, gray: shuffles).*

lated evoked ΔF/F based on the combination of choices and outcomes. Then, we expressed each glomerulus' tuning relative to its position and choice direction. In this analysis, the "preferred reorientation" ("pref. reor.") condition includes responses from the left glomerulus^{ilPN} during CW choices and the right glomerulus^{ilPN} during

CCW choices, categorized by different outcomes. Conversely, the "opposite reorientation" ("opp. reor.") condition groups responses from left glomerulus^{iIPN} during CCW choices and right glomerulus^{iIPN} during CW choices. This analysis revealed clear anatomical structuring (Figure 2e) suggesting an underlying lateralized circuit architecture.

The difference in evoked activity between opposite reorientations (CCW and CW) with and without thermal feedback, suggests that these neurons act as coincidence detectors of specific motor actions and sensory feedback. To test whether this observation is a general feature in our dataset, we designed an index (multiplication index or MI, see Methods) specifically tailored to test this form of multiplicative responses. An MI close to zero indicates a canonical sensory neuron (responses to temperature increase without choice tuning) or an additive interaction between the sensory and motor variables. A positive MI indicates multiplicative interaction, whereas a negative MI suggests directional choice modulation without thermal feedback. This analysis revealed an MI of 1.413, corresponding to a $\sim$4-fold increase in activity when the preferred choice was followed by temp$_{UP}$ (Figure 2f).

We next imaged the somatic activity of iIPN shell neurons (here for brevity referred as iIPN), Figure S6a, n = 17 animals) and compared it with the activity in the r-dHb. The MI distribution of r-dHb neurons was cen-

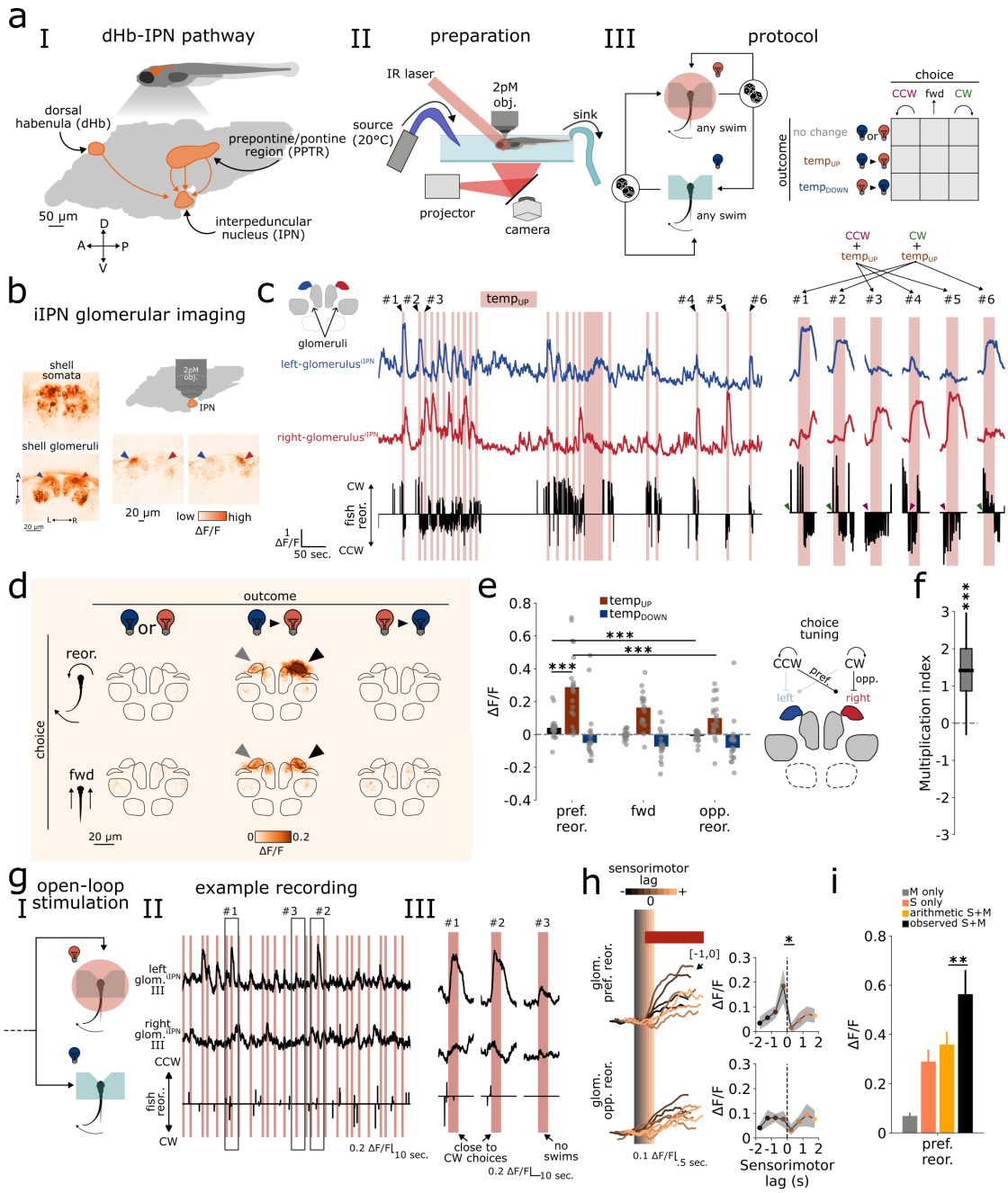

Figure 2: *Emergence of choice-outcome coding in an iIPN glomerulus*

tered at zero, suggesting either a linear summation of choices and outcomes or, most likely, canonical sensory responses. In contrast, iIPN population activity was shifted toward positive values, supporting the previously observed multiplicative responses (Figure S6b-c). Finally, we tested whether iIPN temperature modulation depends on the dHb. We repeated the dHb chemogenetic ablation and after 1 day of recovery, we imaged iIPN neurons (Figure S6d). Compared to controls, dHb ablation significantly reduced the magnitude of evoked ΔF/F (Figure S6e).

We next examined how glomerulus^{iIPN} behaves during an open-loop protocol in which action and sensation are not synchronized (Figure 2gI). We increased temperature for 10 seconds with randomized inter-trial intervals of 10, 20, 30, or 40 seconds (n = 21 animals). We observed that sporadic trials evoked clear calcium transients, particularly when the fish swam close to temp$_{UP}$ (Figure 2gII-III). We computed the evoked ΔF/F as a function of the lag between motor and sensory events (sensorimotor lag), where negative lag values indicated that temp$_{UP}$ followed the swim, and positive values indicated the opposite, with the absolute value representing the lag interval (see Methods, Figure S6f left). This analysis is crucial for determining how sensory and motor events are integrated. A neuron acting as a coincidence detector would show a symmetric response profile around zero lag, whereas a sequence detector would display an asymmetric response (Figure S6f right). Strikingly, the glomerulus^{iIPN} responded strongly when the preferred choice event preceded the sensory event by one second (Figure 2h). This response was not symmetric around zero, indicating that these neurons detect sequences rather than coincidences. Finally, we evaluated glomerular responses during the preferred choice direction closely followed by temp$_{UP}$ (< 1 second) and compared it with the arithmetic sum of the choice-only and temperature-only responses (see Methods). We found that addition alone cannot account for glomerular responses (Figure 2i), further supporting a multiplication hypothesis.

Overall, our imaging results revealed a significant transformation between r-dHb and iIPN neurons. While r-dHb activity signals temperature changes, the iIPN reports which choice caused a temp$_{UP}$ by multiplying the choice and outcome variables. Furthermore, choice-outcome coding is localized to a specific iIPN glomerulus. This, together with the lateralized choice-tuning, strongly suggests a well-defined circuit underlying this computation.

Cytoarchitecture of the iIPN

To elucidate the circuit organization underlying glomerular activity, we started by reconstructing 63 neurons within the right shell subregion from an SBEM dataset [29] (Figure 3a), starting with the ventral-most neurons and extending to the dorsal IPN region (dIPN). Most reconstructed neurons did not cross the midline (Figure 3b first column), had a single dendritic tree, and their axons exhibited minimal, if any, branching.

We first selected reconstructions whose dendrites were located inside the IPN neuropil (41/63). The 87% (36/41) consisted of bipolar neurons with dendrites within the IPN neuropil and whose axons extended outside of it (Figure S7a-b). This group included most neurons with somata located in the intermediate and ventral IPN shell, as well as approximately half of those in the intermediate and dorsal innermost parts of the shell. Most of the axons extended dorsally, posteriorly, and ipsilaterally, reaching a neuropil region near the dorsal raphe nucleus (DRN) (Figure 3a first column). Although these neurons projected outside the IPN, they remained close, still within rhombomere 1. Their tufted dendritic branches were limited in extent, covering an area approximately the size of their soma.

To identify glomeruli, we performed DBSCAN cluster-

Figure 2: ***(a)*** *I: Schematic of the dHb-IPN pathway. II: Head-fixed preparation for imaging experiments. The fish is head-fixed in low-melting point agarose in a petri dish, with the IR laser targeting it. The tail remains free to move and is recorded by a camera. Tail oscillations are analyzed in real time to update both the laser state and the visual stimulus. A perfusion system maintains the petri dish temperature at 21 °C. III: Protocol structure: Temperature changes are stochastically triggered at swim termination, allowing the evaluation of multiple choice-outcome combinations.* ***(b)*** *Left: Two horizontal sections of the transgenic line used. Imaging was performed on iIPN dendrites (bottom image). Right top: schematic of glomeruli^{iIPN} 2-photon calcium imaging experiments. Right bottom: Two example frames during imaging experiment. Studied glomeruli are indicate by the blue (left glomerulus) and red (right glomerulus) arrows.* ***c)*** *Left: example traces from the left (blue) and right (red) glomerulus^{iIPN}. The black trace below represents the animal's behavior, with upward and downward spikes indicating CW and CCW reorientations, respectively. Green and magenta arrowheads point to CW+temp$_{UP}$ and CCW+temp$_{UP}$ events, respectively. Right: magnified choice-outcome events along with glomerular activity.* ***(d)*** *Average ΔF/F projection across choice-outcome combinations. Rows represent choices, and columns represent outcomes. CCW and CW choices have been pooled together by flipping the stack along the midline. In this way, responses for the preferred choice can be seen on the right side, while responses to the opposite choice are on the left.* ***(e)*** *Left: anatomical-based quantification. Blue: temp$_{DOWN}$. Brown: temp$_{UP}$. Black: no temperature change. pref. reor.: contralateral reorientation relative to the glomerulus' anatomical position. fwd: forward swim. opp. reor.: ipsilateral reorientation relative to the glomerulus' anatomical position. Each dot represents a single fish, with bars indicating the median across fish. Right: Schematic of glomerulus^{iIPN} choice-tuning.* ***(f)*** *Multiplication index for the glomeruli^{iIPN}.* ***(g)*** *I: Schematic of open-loop experiment. II: Example recording from the left (top) and right (bottom) glomerulus^{iIPN}. III: Magnified view of the events indicated by gray boxes in II (#1, #2, #3).* ***(h)*** *Glomerular^{iIPN} responses at different sensorimotor lags. Colors depict different sensorimotor lag bins. Lags are color-coded from black (negative lag, choice precedes outcome) to yellow (positive lag, opposite scenario). Left: Triggered average for different bins across fish. Right: Peak ΔF/F (mean ± s.e.m.) for different bins.* ***(i)*** *ΔF/F (mean ± s.e.m.) responses for the preferred choice that was not followed by temp$_{UP}$ (motor only or M only, gray bar), temp$_{UP}$ that was not preceded by any swim (sensory only or S only, pink bar), arithmetic addition of the two (sensory + motor or arithmetic S + M, yellow bar) and the observed responses when preferred choices are followed within 1 second by a temp$_{UP}$ (observed sensory + motor or observed S + M, black bar).*

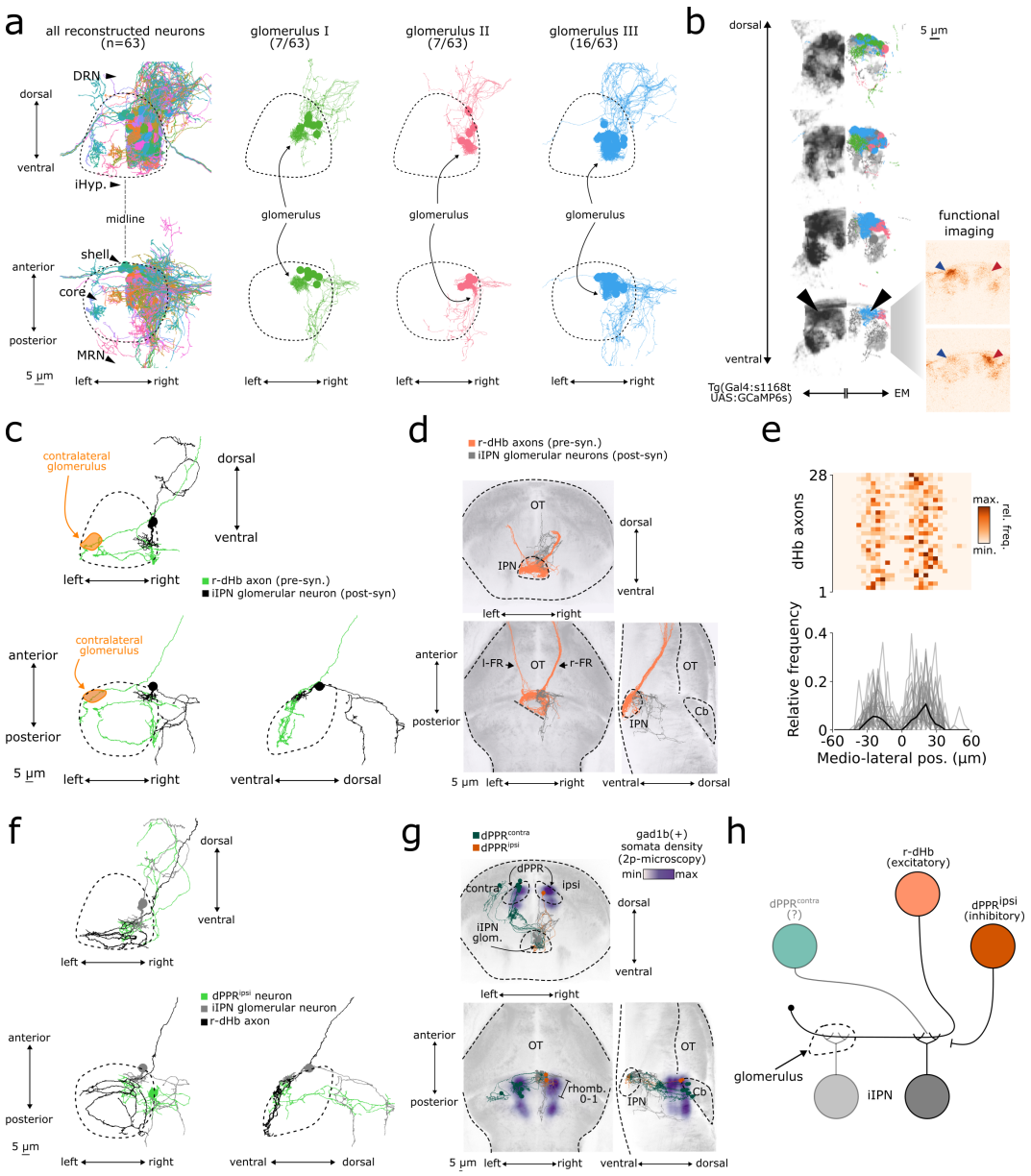

Figure 3: ***Circuit organization***

ing based on dendrite centroid positions (ε =4.5 µm, min. samples=5 neurons). In line with known IPN anatomy [26] we identified three clusters (glomeruli) comprising 7, 7, and 16 neurons, along with 12 outliers (Figure 4a second, third and fourth columns). Coregistration of the EM and imaging data highlighted the third cluster (blue neurons in Figure 3b) as the anatomical substrate of what we previously called the glomeruli^{iIPN}.

Glomerulus^{iIPN} circuit organization

To formulate an implementation hypothesis, we detected axo-dendritic contacts from 4 previously identified neurons and reconstructed their presynaptic partners and other neurons terminating in the glomerulus (see Methods). A significant portion of these inputs originated from dHb neurons (n=39; 35 from r-dHb and 4 from l-dHb, including fully and partially reconstructed neurons, Figure 3c-d). These axons wrap around the iIPN neuropil and innervate multiple regions, including the area corresponding to the contralateral glomerulus. To quantify this observation, we detected synapses on the anterior iIPN (Figure S7c, see Methods), encompassing both the left and right glomerulus^{iIPN}, and plotted their distribution along the mediolateral axis (Figure 3e), confirming that dHb axons innervate both glomeruli^{iIPN}.

A second group of the presynaptic partners (n = 5 neurons) consisted of unipolar neurons from the dorsal- and anterior-most part of the contralateral dPPR (relative to the reconstructed region, dPPR^{contra}). Unlike dHb axons, their axon terminals had tufted endings resembling iIPN dendrites and exclusively terminated on the seed glomerulus (Figure S7d-e). Additionally, we identified an ipsilateral unipolar dPPR neuron (n = 1 neuron, dPPR^{ipsi}) projecting in the glomerulus that did not contact seed

neuron dendrites (initially reconstructed as iIPN postsynaptic partner, Figure 3f). Overlaying gad1b(+) cell density with all reconstructed dPPR neurons revealed close alignment, suggesting that some of these neurons might be inhibitory (Figure 3g).

To validate the EM reconstructions, we performed photoactivation experiments (Figure S8a, n = 4 animals) using animals coexpressing a photoactivable GFP variant (paGFP) [30] and red-labeled dHb axons. We used the red channel to locate the right glomerulus^{iIPN} and activated the paGFP at 800 nm to retrogradely or anterogradely label neurons with axons or dendrites in the activation region, respectively. Consistent with EM reconstructions, we labeled the somata and axons of glomerular iIPN neurons (Figure S8b, panels I-III), dHb axons (Figure S8b, panel I), dPPR^{ipsi} and dPPR^{contra} neurons (Figure S8b, panels IV and V). Retrograde labeling revealed comparable numbers of dPPR^{ipsi} and dPPR^{contra} neurons (Figure S8d). However, dPPR^{contra} somata were confined to a smaller, more posterior elliptical region, whereas dPPR^{ipsi} somata were distributed in a more diffuse, anterior region (Figure S8b, panels IV and V, Figure S8c). A separate experiment confirmed overlap between the dPPR^{ipsi} and the gad1b marker, verifying the inhibitory nature of some dPPR^{ipsi} neurons (Figure S8e).

To summarize, we found that glomerular iIPN neurons receive three distinct inputs: dHb (predominantly from the right nucleus), dPPR^{ipsi} and dPPR^{contra} (Figure 3h). The dHb is known to be a glutamatergic region and is likely responsible for the temp$_{UP}$ excitation component observed in downstream iIPN neurons. In contrast, The dPPR^{ipsi} sends inhibitory (GABAergic) signals, the role of which is still unclear.

Choice-outcome responses in dHb axon terminals

Based on the morphology of dHb axons and the activity in dHb neurons, we expected symmetric dHb axon activity increases in regions corresponding to both glomeruli at temp$_{UP}$. However, population recordings of dHb axons (n = 9 animals), Figure 4a) revealed heterogeneous activity with marked lateralization[31]. Pixel-wise principal component analysis (PCA, see Methods) highlighted this heterogeneity, showing "patchy" components (Figure 4b). Some components were symmetric around the midline (PC1, PC2, PC4), whereas others were strongly asymmetric (PC3, PC5), with patchy regions overlapping the underlying glomeruli. Analysis of the pixel-wise ΔF/F responses for different choice-outcome combinations revealed a pattern similar to that observed in the glomerulus^{iIPN} (Figure 4c, gray and black arrows in the second column). We then extracted the activity from the glomerulus^{iIPN}-like region and found the same anatomical choice tuning (Figure 4d) and a similar multiplication index (Figure 4e). Interestingly, axon imaging revealed a second medial patch responding to temp$_{DOWN}$ (Figure 4c, light and dark blue arrows in the third column). This activity might be related to a second pair of glomeruli with opposite outcome tuning with respect to the one studied here.

This activity footprint may originate for two different reasons. The first one is due to a small population of dHb neurons having choice-outcome coding that relay this information to the glomerulus with matched choice-tuning. However, this scenario is unlikely as we did not observe this tuning in dHb somatic activity and none of our reconstructed dHb axons project to a specific glomerulus, a result also consistent with the literature [26, 32]. Furthermore, similar patchy structures have been observed during visual stimulation in the dIPN [28] and during recordings of spontaneous activity in the ventral IPN [26]. These results, violate the anatomical prediction of symmetric functional activation of r-dHb axons. A second and more plausible explanation reconciles our anatomical and functional findings through modulation of habenula axon terminals [33].

Modulation via GABA$_B$ receptor (GABA$_B$R) signaling has been reported in both zebrafish [33] and mammals [34–36]. Interestingly, in mammals, GABA$_B$Rs do not reduce dHb glutamate release [37]; instead, they strongly increase it [34–36], resulting in multiplicative-like responses for the same habenular activity. There-

Figure 3: ***(a)*** *iIPN reconstructions. Columns represent all the reconstructed neurons (each color denotes a single neuron, color randomly assigned) and the three identified glomeruli (green: glomerulus I, pink: glomerulus II, blue: glomerulus III, gray: outliers). Frontal projection on the top row and horizontal projection on the bottom row. Dashed regions enclose the IPN neuropil. Reference space from mapZebrain atlas.* ***(b)*** *Co-localization of EM iIPN and s1168t(+) neurons. Left: Tg(s1168t:Gal4; UAS: GCaMP6s) line. Right: EM reconstructions with the same color code as in (a). Arrowhead point to the same positions in the two modalities, where it was previously observed choice-outcome coding (example frames on the right). Reference space from mapZebrain atlas.* ***(c)*** *Exemplar habenula axon with its glomerular iIPN postsynaptic partner. Green: habenula axon. Black: glomerular iIPN neuron. Orange: putative region occupied by the contralateral glomerulus. Top: frontal projection. Left bottom: horizontal projection. Right bottom: sagittal projection. Reference space from mapZebrain atlas.* ***(d)*** *dHb axons (pink) reconstructed as presynaptic partners of seed iIPN neurons (gray). Top: frontal projection. Left bottom: horizontal projection. Right bottom: sagittal projection. The dashed line in the horizontal projection indicates a dataset discontinuity where most of the dHb axons were missed (OT: optic tectum, Cb: cerebellum, l-FR: left fasciculus retroflexus, r-FR: right fasciculus retroflexus). Reference space and anatomy from mapZebrain atlas.* ***(e)*** *Quantification of synaptic contact distribution in the anterior iIPN. Top: Distribution of single axons. Each row represents a dHb axon, and each column represents a bin along the mediolateral axis. Color coding represents relative frequency (from light to dark orange). dHb axons are sorted by the total number of detected contacts. Bottom: Pooled frequency distributions. Each gray line is a single axon, and the mean is shown in black.* ***f)*** *dPPR^{ipsi} axon projecting in the glomerulus (green). As a reference, a dHb axon is shown in black, and an glomerulus iIPN neuron in gray. Top: frontal projection. Bottom left: horizontal projection. Bottom right: sagittal projection. Reference space from mapZebrain atlas.* ***(g)*** *dPPR^{contra} (green) and dPPR^{ipsi} (orange) reconstructions along with glomerular iIPN (gray) neurons. Top: frontal projection. Left bottom: horizontal projection. Right bottom: sagittal projection. In purple, density of gad1b(+) (inhibitory) neurons. (OT: optic tectum, Cb: cerebellum). Reference space and anatomy from mapZebrain atlas.* ***(h)*** *Circuit organization schematic.*

fore, a simple model could be that outcome information is transmitted from r-dHb axon terminals and subsequently modulated at the axon terminals in the iIPN by a hypothetical population of GABAergic choice-neurons, which in turn dictates glomerular^{iIPN} activity (Figure S9a).

We tested this hypothesis using a $GABA_BR$ antagonist (CGP 46381; see Methods). Fish underwent an initial imaging session, after which we applied the antagonist (treatment group, n = 7) or water (control group, n = 9) and then re-imaged the same plane. The treatment had no effect on swim frequency (Figure S9b) or global dHb axon activity, as assessed by pixel-wise ΔF/F standard deviation over the entire experiment (see Methods, Figure S9c-d). We then quantified its effect on the $temp_{UP}$-tuned patch and, for comparison, the $temp_{DOWN}$-tuned patch. Strikingly, $GABA_BR$ blockade abolished choice-outcome responses in the $temp_{UP}$- but not the $temp_{DOWN}$-tuned patch (Figure S9e, Figure 4g), suggesting a specialized role for $GABA_BR$ in shaping $temp_{UP}$-tuned dHb axon activity and consequently choice-outcome coding.

Choice responses in GABAergic dPPR neurons

Previous findings suggest that GABAergic transmission in the glomerulus regulates dHb axon modulation in response to animal choices. Therefore, since dHb axons and iIPN neurons are glutamatergic, we sought to image GABAergic activity in the glomeruli, likely corresponding to $dPPR^{ipsi}$ axon terminals ($glomeruli^{dPPR}$, Figure 4h and Figure S9f, n = 13 animals). $Glomeruli^{dPPR}$ exhibited dynamic, non-stationary activity (Figure S9g). Analysis of choice-outcome combinations revealed no multiplicative responses when considering either $temp_{UP}$ or $temp_{DOWN}$ (Figure 4i) but only a modulation of directional choices overlapped with additive temperature modulation (Figure 4j, Figure S9h-i). Directional choice-tuning mirrored that of iIPN neurons, with excitation for the

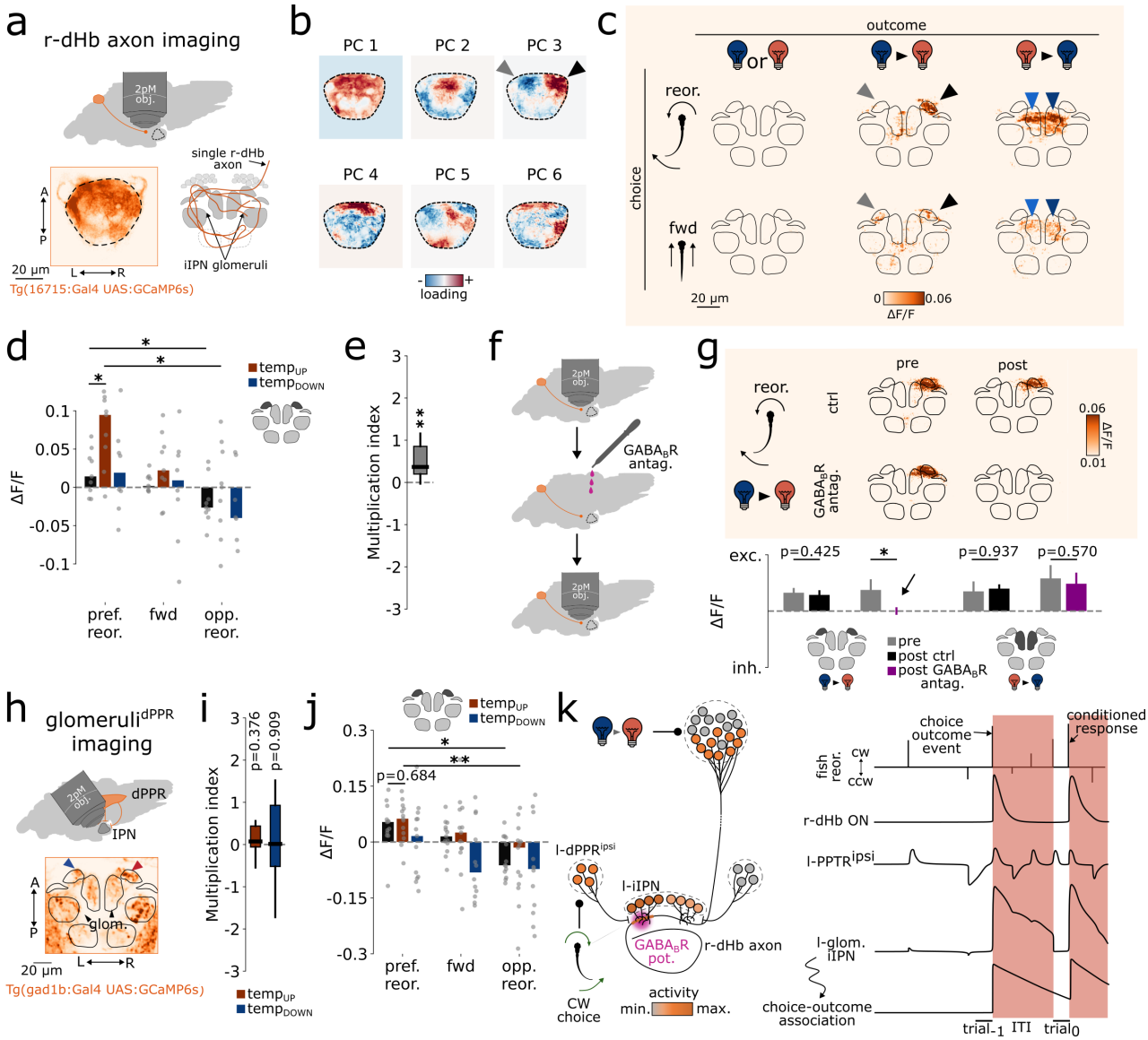

Figure 4: ***A circuit mechanism for credit assignment***

contralateral direction relative to the glomerular hemisphere (CCW for the right glomerulus^{dPPR}, CW for the contralateral counterpart) and inhibition for the opposite reorientation (Figure 4j, Figure S9h).

Based on our anatomy results, we hypothesized that the observed glomeruli^{dPPR} activity reflected dPPR^{ipsi} inputs, predicting similar activity patterns in the corresponding dPPR somata region. To test this, we recorded dPPR neurons at multiple dorsoventral planes using a nuclear-localized calcium sensor expressed panneuronally (Figure S10a, n = 7 animals). To analyze functional activity, we correlated each neuron's activity (n ROIs = 4352 ± 503 per plane, from dPPR and adjacent optic tectum, Figure S10b) with 18 regressors representing sensory, motor, and sensorimotor profiles, including activity observed in glomeruli^{dPPR} (bidirectional choice modulation, see Methods). For each neuron, we calculated correlation coefficients and p-values through circular permutation of calcium traces, assigning neurons to regressors with significant correlations ($p < 0.05$) above a fixed threshold ($r = 0.3$). We then filtered the ROIs based on spatial consistency across fish (across fish radius search = 10 µm) and repeated this process for the left and right hemispheres (see Methods). This analysis revealed two distinct neuron populations bidirectionally modulated by choice direction (Figure S10c, Figure S10d-f for other maps). One population located in rhombomeres 2 and 3, was ipsilateral to the turn direction. The second population was contralateral, positioned in a more anterior and dorsal region, near the reconstructed dPPR^{ipsi} neurons.

A circuit model for behavioral credit assignment

How do larval zebrafish link action and outcome to drive adaptive behavior? We propose that positive gain modulation (or potentiation) of dHb-to-iIPN transmission plays a central role in choice-outcome coding. This modulation is mediated by dPPR^{ipsi} neurons, which release GABA in the glomerulus in a choice-specific manner. GABA released through direct synaptic connections or non-synaptic volume transmission [33], potentiates glutamatergic transmission from the dHb to iIPN neurons. In the context of our paradigm, this circuit could function as follows.

The r-dHb transmits fast-adapting temperature ON glutamatergic signals (Figure S4f). In the absence of an animal's choice (for example, during externally induced temperature changes), this excitation is weak, resulting in minimal activation of the glomeruli^{iIPN} (Figure S11I, Figure 2i pink bar). Upon a directional choice, for example a CW turn, left dPPR^{ipsi} neurons increase their firing (Figure 4i, Figure S9h) activating GABA$_B$Rs on habenula axon terminals in the right hemisphere. Simultaneously, right dPPR^{ipsi} neurons reduce their firing, downmodulating habenula axon terminals on the contralateral hemisphere. This modulation can be seen as an elegibility trace for incoming sensory signals. If no sensory consequence follows the choice (no temperature change), this modulation remains unexpressed, leading to only minimal activation of the glomeruli^{iIPN} (Figure S11II, Figure 2e black bar pref. reor., Figure 2i gray bar). However, if r-dHb is excited shortly after the choice (temp$_{UP}$), the potentiation becomes expressed. This results in enhanced glutamatergic release in the left glomerulus^{iIPN}, producing multiplicative-like responses in axon terminals (Figure 4c-e) and local iIPN neurons (Figure 4k left, Figure 2d-f). This mechanism could explain the observed asymmetry in dHb axons and glomeruli^{iIPN}, sensory responses in r-dHb somata and choice responses in dPPR^{ipsi} neurons.

Through this circuit, larval zebrafish could create an internal representation of the last choice-outcome relationship. This would allow the animal to, through a yet undetermined mechanism, induce turning in the correct direction to respond to future opposite temperature changes (temp$_{DOWN}$, Figure 4k right).

Discussion

In the present study, we describe how the brain of larval zebrafish links, at the circuit level, relevant behavioral choices to sensory consequences. Using an operant thermoregulatory task [7–13], we found that fish

Figure 4: ***(a)*** *Top: Schematic of 2-photon calcium imaging experiments in dHb axons. Left bottom: Sum projection from an example recording. Right bottom: Schematic of dHb axon morphology.* ***(b)*** *Pixel-wise PC analysis. Loadings of the first 6 PCs are shown from blue (negative) to red (positive).* ***(c)*** *Average ΔF/F projection across choice-outcome combinations. Rows represent choices, and columns represent outcomes. CCW and CW choices have been pooled together by flipping the stack along the midline. In this way, responses for the preferred choice can be seen on the right side, while responses to the opposite choice are on the left.* ***(d)*** *Anatomical-based quantification. Blue: temp$_{DOWN}$. Brown: temp$_{UP}$. Black: no temperature change. pref. reor.: contralateral reorientation relative to the underlying glomerulus' anatomical position. fwd: forward (fwd) swim. opp. reor.: ipsilateral reorientation relative to the underlying glomerulus' anatomical position. Each dot represents a single fish, with bars indicating the median across fish.* ***(e)*** *Multiplication index for glomeruli^{dHb}.* ***(f)*** *Schematic of pharmacology experiments.* ***(g)*** *dHb axon activity upon GABA$_B$R antagonist treatment. Top: Average ΔF/F projection during reorientation followed by temp$_{UP}$. Rows represent experimental groups (first row: ctrl group, second row: treatment group) and columns represent experimental timepoint (first column: first imaging session, second column: second imaging session). Bottom: ΔF/F quantification (mean ± s.e.m.) for the lateral (responding to temp$_{UP}$) and medial (responding to temp$_{DOWN}$) for the respective preferred choice and outcome condition, for different experimental groups. (gray bars: first imaging session, black bar: second imaging session ctrl group, purples bars: second imaging session treatment group).* ***(h)*** *Top: Schematic of 2-photon calcium imaging experiments in glomeruli^{dPPR}. Bottom: Sum projection from an example recording.* ***(i)*** *Multiplication index when considering either temp$_{UP}$ (brown) or temp$_{DOWN}$ (blue) outcomes.* ***(j)*** *Anatomical-based quantification. Blue: temp$_{DOWN}$. Brown: temp$_{UP}$. Black: no temperature change. pref. reor.: contralateral reorientation relative to the underlying glomerulus^{dPPR}'s anatomical position. fwd: Forward swim. opp. reor.: ipsilateral reorientation relative to the underlying glomerulus^{dPPR}'s anatomical position. Each dot represents a single fish, with bars indicating the median across fish.* ***(k)*** *Summary model.*

adaptively select the best motor output (CCW or CW turnings) to avoid aversive thermal conditions. This behavior was dependent on the temporal relationship between the choice and the thermal feedback [38]. Chemogenetic ablation of the dHb impaired the fish's ability to adapt behaviorally but spared innate temperature responses. This suggests that the dHb, and the downstream interpeduncular nucleus (IPN), are not involved in sensory processing or innate sensorimotor transformations but play a role in using prior experience to guide behavior. These results are supported by previous studies linking this pathway to fear and avoidance learning [20–23, 34, 39, 40], experience-dependent navigation [17], learning of directional rules [41] and generally support the idea of the dHb as an experience-dependent switchboard of behavior [15].

Using calcium imaging, we show that, when fish succeed in raising the temperature (positive valence outcome), a population of neurons in the intermediate IPN (iIPN), reported which motor choice lead to that sensory consequence (choice-outcome coding) through multiplicative-like responses. Neurons reporting the same action where clustered together, on the opposite hemisphere relative to the preferred choice direction. Furthermore, they extended their dendrites in an ipsilateral neuropil region called glomerulus [26].

Further experiments are needed to assess whether neurons in this glomerulus are specialized for temperature sensing or are multimodal [17]. The former hypothesis seems unlikely, as it is known that dHb projections carry odor information [42] and other variables [17, 43, 44]. An intriguing alternative could be that the glomerular organization groups iIPN neurons based on choice modulation, rather than sensory modality. Different neurons within this glomerulus could receive near-random habenula inputs representing multiple sensory modalities or stimulus statistics. As a result, each iIPN neuron could become maximally excited by a unique combination of sensory outcomes generated by a specific action. For example, one neuron could respond most strongly to a left turn choice followed by an increase in both temperature and luminance, while another could respond when the same movement is followed by a simultaneous increase in temperature and aversive odor concentration. Such coding would enable the animal to form multimodal associations with its environment.

Next, we leveraged an electron microscopy dataset to reconstruct the entire circuit associated to the functionally identified glomerulus. The most prominent input comes from the dHb. These terminals originate from both habenulae, although predominantly from the right nucleus [26, 45, 46]. All the dHb axons exhibit the characteristic ring-like morphology previously described [26, 46]. Assuming that glomeruli are the basic computational units of the IPN, dHb axons appear to broadcast the same information to multiple glomeruli in parallel, suggesting a one-to-many connectivity. In line with this, we found synaptic contacts both on the right (reconstructed hemisphere) and on the left glomerulus. At the functional level we observed, in the dHb cell somata, both ON and OFF responses to temperature with different temporal profiles, which are likely transmitted directly from the olfactory bulb [17, 47–51]. Strikingly, when we imaged axon terminals of the same neurons we found lateralized patch-like patterns overlapping with the underlying glomerulus [26, 28, 31] and with the same choice-outcome coding. Thus, the multiplication of sensory and choice signals does not occur in iIPN neurons but rather in the r-dHb presynaptic axon terminals. Notably, presynaptic modulation of sensory axon is an elegant and efficient mechanism for linking choice and outcome, requiring only one sensory neuron, with different axon segments modulated independently by distinct decisions of the animal or body contexts. For instance, here a single dHb axon could target both the left and right glomerulus^{iIPN} through en passant synapses [52].

The other major input stream to the iIPN neurons originates from the dPPR [24, 26, 40, 45, 53–55], a region that has been extensively linked to exploratory [56] and stimulus evoked tail [31, 57–59] and eye movements [60]. In contrast to the dHb axons, both dPPR populations were glomerulus specific. One originates from the ipsilateral (dPPR^{ipsi}) hemisphere and the other originates from the contralateral (dPPR^{contra}) hemisphere with respect to the target glomerulus position. dPPR^{contra} neurons form axo-dendritic contacts with iIPN neurons whereas dPPR^{ipsi} neurons do not. While both populations overlap with GABAergic nuclei, we found direct evidence for gad1b(+) expression in the dPPR^{ipsi} only. Quite strikingly, imaging of the dPPR^{ipsi} GABAergic terminals in the glomerulus revelaed modulation of activity aligned with behavioral choices, regardless of the sensory consequence. Furthermore, choice tuning was aligned with the positive modulation observed in the other circuit components. If this was a case of presynaptic inhibition, we would have expected the activity of this population to be tuned to the opposite behavioral choice to inhibit dHb terminals for ipsilateral turns. Instead, our data suggests that GABA may act as a positive gain modulator through $GABA_BR$ signaling. This hypothesis was confirmed by pharmacology experiments. Importantly, this does not exclude additional mechanisms, such as postsynaptic inhibition [61], intrinsic properties of iIPN neurons or other forms of neuromodulation [62, 63]. In mammals, a prominent enhancement of neurotransmitter release from the medial habenula (mHb, the homolog of the zebrafish dHb) to IPN neurons, driven by presynaptic $GABA_BR$ activation has been described [34, 35, 64–66]. Importantly, this potentiation mechanism is specific to IPN subregion [67] and cell-type specific [36]. This seems to be the case for larval zebrafish as well, as $GABA_BR$ signaling it was recently shown to play a role in trans-inhibition across IPN subregions [33].

Although potentiation in the mammalian IPN has been extensively studied [34–36, 64–67], its functional role within the mHb-IPN circuit remains unknown. The mechanism identified here may serve a similar function in mammals, a hypothesis that can be experimentally tested. To conclude, while implementation details might be specific to this circuit, modulation of sensory axons by choice neurons might be a more general principle adopted by other brain circuits.

Acknowledgements

The authors thank the members of the Portugues lab for constructive discussions throughout the project. In

particular, we want to thank You Kure Wu for the constant technical and scientific support. We also thank Thomas Frank, Thomas Misgeld and especially Ilona Grunwald Kadow for the support and constructive feedback received during the project. This research was funded by the German Research Foundation (DFG) through SPP 2205 (project 430156228), Germany's Excellence Strategy within the framework of the Munich Cluster for Systems Neurology (EXC 2145 SyNergy, identifier 390857198), through the "Enhanced resolution microscopy" (project 518284373), by the Volkswagen Stiftung via a Life? grant and by the Max Planck Gesellschaft.

Contributions

EP, VP and RP designed the project. EP built the IR laser freely swimming and head-fixed rigs with support from VP. EP performed the experiments, with the support of VP (during iIPN somata imaging and initial freely-swimming experiments) and the support of AS (for dHb chemogenetic ablations and anatomies). EP performed all analysis and quantifications. EM reconstructions were done by ariadne.ai AG and in a small amount by EP. EP, VP and RP wrote the manuscript.

Competing interests

The authors declare no competing interest.

Materials and Methods

Zebrafish husbandry

All procedures related to animal handling were conducted following protocols approved by the Technische Universität München and the Regierung von Oberbayern (TVA 55-2-1-54-2532-101-12 and TVA 55.2-2532.Vet_02-24-5). Adult zebrafish (Danio rerio) from Tüpfel long fin (TL) strain were kept at 27,5-28°C on a 14/10 light cycle, and hosted in a fish facility that provided full recirculation of water with carbon-, bio- and UV filtering and a daily exchange of 12% of water. Water pH was kept at 7,0-7,5 with a 20 g/liter buffer and conductivity maintained at 750-800 µS using 100g/liter. Fish were hosted in 3,5 liter tanks in groups of 7-17 animals and fed with Gemma micron 300 (Skretting USA) and live food (Artemia salina) twice per day. Larvae were fed with Sera micron Nature (Sera) and ST-1 (Aquaschwarz) three times a day. All experiments were conducted on 5-8 dpf larvae of yet undetermined sex. The week before the experiment, one male and one female or three male and three female animals were left breeding overnight in a sloping breeding tank or breeding tank (Tecniplast). The day after, eggs were collected in the morning, rinsed with water from the facility water system, and then kept in groups of 20-40 in 90 cm Petri dishes filled with Danieau solution 0.3x (17.4 mM NaCl, 0.21 mM KCl, 0.12 mM $MgSO_4$, 0.18 mM $Ca(NO_3)_2$, 1.5 mM HEPES, reagents from Sigma-Aldrich) until hatching and in water from the fish facility afterwards. Larvae were kept in an incubator at 28,5°C and a 14/10 hour light/dark cycle, and their solution was changed daily. At 4 or 5 dpf, animals were lightly anesthetized with Tricaine 440 mesylate (Sigma-Aldrich) and screened for fluorescence under an epifluorescent microscope.

Animal strains

The Tuepfel long-fin (TL) wild-type strain was used for freely swimming experiments. For imaging experiments, fish were mitfa -/- (i.e., nacre) mutants lacking melanophores to allow optical access to the brain. Transgenic lines used are:

- Tg(16715:Gal4);Tg(UAS:Ntr-mcherry) [17] used for dHb ablation and targeted photoactivation experiments
- Tg(16715:Gal4);Tg(UAS:GCaMP6s)mpn101 [17, 68] used for dHb somata and axons imaging experiments and anatomies
- Tg(elavl3:GCaMP6s) [69] used for dHb somata imaging experiment
- Tg(evavl3:Hsa.H2B-GCaMP6s) [70] used for iIPN and dPPR somata imaging experiments
- Tg(s1168t:Gal4);Tg(UAS:GCaMP6s)mpn101 [27, 68] used for iIPN dendrites (glomeruli^{iIPN}) imaging experiment and anatomies
- Tg(gad1b:Gal4);Tg(UAS:GCaMP6s)mpn101 [68, 71] used for dPPR axon (glomeruli^{dPPR}) imaging experiments and anatomies
- Tg(Cau.Tuba1:c3paGFP)a7437 [30] used for photoactivation experiments
- Tg(gad1b:Gal4);Tg(UAS:mCherry) [72] for anatomy and targeted photoactivation experiments.

Experimental Setups

IR laser freely swim setup

This setup was inspired by a previous publication [16] and largely follow the same design. Briefly, fish were placed in an arena 200 mm x 110 mm (cold avoidance experiment) or 200 mm x 65 mm (operant thermoregulatory experiments), illuminated with 750 nm IR illumination, and allowed to move freely. For all experiments, we projected a visual pattern (Optoma) on the arena floor, following pink noise statistics [24] in spatial frequencies, to provide the fish with additional self-motion cues. The fish were tracked at 150 Hz (camera: ximea USB3.0 MQ022RG-CM, objective: 25 mm Edmund Optics objective) using Stytra [17, 31, 73], from which body position and heading were extracted. Positional data controlled the angles of two scan mirrors (Thorlabs, GVS102) controlled by an DAQ board (National Instruments, 781438-01), maintaining a 980 nm laser beam centered on the fish's center of mass. Based on the experimental condition, the laser beam was either centered on the fish ($temp_{UP}$ condition) or redirected to a distant heat sink outside the behavioral arena ($temp_{DOWN}$ condition). This approach minimized delays and gradual ramp-ups in laser power. $Temp_{UP/DOWN}$ conditions varied depending on the specific experiment. In front of the

camera we additionally placed a 800 nm shortpass filter (Thorlabs, ESH0800) and a 650 nm longpass filter. For calibrations, we fixed a thermocouple [17] to the behavioral arena and filled it with water. Then, the laser beam was rapidly moved on the thermocouple or on a 5 mm distant region. Temperature was recorded with a temperature controller (Warner Instruments, CI 100) connected to the behavioral PC through a LabJack series U3-LV (LabJack) [17].

IR laser setup for two-photon microscopy

The same IR laser was positioned in front of a 1-axes galvanometric mirror, which switched between two states. In one state, the mirror directed the beam toward the fish, positioned frontally at an angle that avoided the objective and allowed the beam to reach the fish body. In the second state, the mirror redirected the beam to a heat sink distant from the animal. This setup enabled a rapid temperature increase without the need for excessively high laser power. To filter out potential contaminants detected by the microscope's photomultipliers, we placed a 750 nm long-pass filter (Thorlabs, FELH0750) in front of the IR laser. In order to avoid temperature accumulations, the laser power used was reduced to 1/3 of the one used for freely swim experiments. Furthermore, the fish was perfused with 20 °C water as previously done [17]. We presented visual stimulation at 40 Hz (Asus P2E microprojector). A red longpass filter (Kodak Wratten No.25) allowed the simultaneous 905 nm imaging and visual stimulation. Fish were illuminated using infrared light-emitting diodes (850 nm wavelength) and imaged from below at 200 Hz (Pike F032B, Allied Vision Technologies).

Two-photon microscopy

Functional imaging data were acquired at 2-5 Hz, depending on the calcium sensor kinetic being used in the experiment. Laser power and field of view were adjusted based on the particular structure being imaged. For anatomical data, we acquired 10 frames (1Hz rate for 10 seconds) per plane with a 1-2 microns inter-plane distance. Once a plane was imaged, the objective was moved by 1 micron and the acquisition restarted. Dual channel (red and green) anatomical stacks were acquired at 950-1000 nm while single channel ones (only green) at 905 nm.

Animal preparation and behavioral protocols

All experiments where behavior was recorded were run from 10.00 h to 20.00 h, room temperature was set to 20/21 °C. All visual and thermal stimulus presentation as well as behavioral tracking were performed using Stytra package [73].

Cold avoidance experiment

Here, the IR laser state ($temp^{UP/DOWN}$) was dependent on the fish being inside an experimentally defined rectangular region (ROI)[74]. Such a region was invisible to the fish and once inside, a whole-body temperature increase was produced through the IR laser.

Operant thermoregulatory assay

This protocol [10] was designed to test whether zebrafish can associate a directional choice with a specific temperature consequence. The first experiment presented comprised 60 trials: 30 trials where an increase in temperature was paired with a turn in a designated 'rule direction' (either CCW or CW), and 30 trials in the opposite direction. For delay and dHb ablation experiments we did 10 trials per block, as previous results highlighted a short- and not a long-term memory process building over many trials. When inside an experimentally defined region (not close to arena borders) a trial starts by decreasing the temperature ($temp_{DOWN}$) at the end of a swim of any kind (CCW, forward or CW). Then, the animal can increase the temperature again by turning toward the rule direction. The trial ends when the fish turns in the rule direction or after 10 seconds from $temp_{DOWN}$ elapsed (timeout). Then, after a minimum ITI of 5 seconds (where the laser is directed toward the animal) and the fish being away from the border, the next trial starts. As this was a self-paced experiment, its duration varied between fish. All temperature transitions were triggered by the animal's movement, as we observed a net decrease in swim rate otherwise [38]. Fish were tested once, between 5 and 8 days post-fertilization (dpf), and otherwise kept in an incubator at 28 °C near the behavioral apparatus. Performance did not significantly differ with age.

2-photon imaging behavioral protocol

This protocol was designed to assess the combined effects of choices and thermal consequences on different neuronal populations. For imaging of iIPN somata, temperature changes were stochastically triggered at the end of swim events, with a 25% probability that each swim would switch the current laser state. In the rest, a similar protocol was applied, but once the laser turned ON, it remained ON for a minimum of 10 seconds. The first swim after this interval turned the laser OFF, initiating another 10 second long refractory period. After this, each swim had a 0.3 (30%) probability of turning the laser ON again. This modification ensured relatively frequent temperature increases while allowing sufficient time between changes to facilitate clear baseline extraction and quantification. Throughout the entire experiment we also presented whole field forward motion at 3 mm/s to promote swimming events with rotational as well as translational visual feedback. Translational and rotational feedback were computed online as previously done [24]. The experiment lasted either 30 minutes or 1 hour ($glomeruli^{dPPR}$ imaging) and only one plane was acquired per each fish. If during the experiment the acquisition drifted, the experiment was restarted for a maximum of three times.

Head-fixed preparation

For functional imaging experiments, fish were embedded in 2.5% low-melting point agarose in 30 mm petri dishes. The agarose around the tail and nose was removed with a scalpel to allow tail movements and direct stimulation of the olfactory bulb [17, 44]. Once the animal was placed under the objective, we waited 5-10 minutes with the fish engaged in the same visual closed-loop that will experience later. For anatomical experiments, fish were embedded in 1.5%/2% low-melting point agarose in 30 mm petri dishes.

Manipulations

Chemogenetic ablation

Targeted dHb ablation was performed using the Nitroreductase (Ntr)-Nifurpirinol (NfP) chemogenetic approach [75]. Ntr catalyzes the reduction of the pro-drug NfP into a cytotoxic compound, leading to cell death. By expressing Ntr in specific cells, targeted ablations can be achieved. We used the Tg(Gal4:16715):Tg(UAS:Ntr-mCherry) line [17], which selectively expresses Ntr-mCherry in the dorsal habenula of larval zebrafish. Larvae were first screened for mCherry expression using an upright epifluorescence microscope. mCherry-positive larvae (ablation group) and mCherry-negative larvae (treatment control group) were then placed in separate 90 mm Petri dishes containing minimal water. Subsequently, 30 mL of a 5 µM NfP solution with 0.2% DMSO (diluted 500 times from a 2.5 mM NfP stock) was added to each dish. The Petri dishes were incubated in a dark box at 28°C for 16 hours to prevent degradation of the photosensitive NfP. Both the preparation of the NfP solution and the transfer of fish were also conducted in the dark to minimize NfP degradation. After the incubation period, larvae were removed from the solution and thoroughly washed three times to eliminate any residual NfP and DMSO. The fish were then left to recover in fish water for one day. Behavioral experiments were conducted before and after ablation to assess functional changes due to dHb neuron loss. To evaluate the efficiency of dHb ablation, random larvae were selected before and after treatment and imaged using a confocal microscope to assess mCherry expression in dHb neurons.

Pharmacological blockade of $GABA_B$Rs

We used the $GABA_B$R antagonist CGP 46381 (CAS 123691-14-5, Santa Cruz Biotechnology). After a first imaging session (as described elsewhere), head-fixed fish were brought under a stereomicroscope close to the experimental rig. Then, we carefully washed for three times with either water (ctrl group) or 50 µM CGP 46381 (treatment group) using a pasteur pipette. Fish was subsequently moved again in the two-photon microscope rig, let habituate to the visual closed-loop and allow for drug diffusion for 10 minutes, and started the second imaging session. Fish were used only once. In this experiment, bath application was necessary, as intraventricular injections completely abolish fish swimming behavior, particularly immediately after injection.

Anatomical registration

Registrations were done using a combination of manual and automatic procedures using the free Computational Morphometry Toolkit (CMTK - http://www.nitrc.org/projects/cmtk) (volumetric data) or the python package dipy. Each single-plane dataset with the exception of r-dHb somata imaging have been morphed with an internal reference, to allow for average ΔF/F projections and quantifications. All volumetric data (EM, photoactivations, anatomies and multiplane dPPR population imaging) have been morphed to the Max Planck Zebrafish Brain Atlas mapzbrain (https://mapzebrain.org) [76] for visualizations and quantifications.

Data analysis

All analyses were performed using Python 3.8 and relevant Python libraries for scientific computing, like numpy, scipy and scikit-learn.

Preprocessing of behavioral data

Relevant behavioral parameters were tracked online using Stytra [73]. All the behavioral preprocessing was performed using the python package Bouter (https://github.com/portugueslab/bouter) and as previously described [17, 24, 31]. For head-fixed experiments reorientation angle was computed as the cumulative tail bending over the first 70 ms from swim onset [77] while for freely swimming experiment the cumulative reorientation from swim start to end. To categorize CCW, forward and CW swims in head-fixed experiments we set a threshold of 10 degrees.

ROI occupancy

In Figure S1f, we report ROI occupancy as a measure of cold avoidance behavior. If the fish exhibit cold avoidance, they will spend more time in the warmed region. ROI occupancy was computed as the fraction of time spent inside the ROI over the entire experiment duration, multiplied by 100.

Outside ROI exposure time

In Figure S1g, we report the outside ROI exposure time as another measure of cold avoidance. For each instance, we computed the time spent from ROI exit to re-entry and then averaged this value per fish.

Angular velocity

In Figure 1c and Figure S2c, we report the angular velocity at temperature transitions during the operant assay. Angular velocity was computed by first smoothing the fish heading using a Savitzky–Golay filter (window = 150 ms), then calculating the first-order derivative and dividing it by the time interval between consecutive timepoints. Conditioned responses were evaluated by measuring the average angular velocity (baseline-subtracted) from 0.5 to 0.9 sec. after $temp_{DOWN}$.

Reorientation bias

In Figure 1d,g,l and Figure S2e,f we report reorientation bias as an index of task performance. This was defined as the average reorientation angle of the first swim detected after $temp_{DOWN}$ for trials where the preceding ITI was lower (or higher for Figure S2f, yellow) than 7.5 sec (except for Figure 1d). For Figure S2e we considered all the swims during ITIs. For shuffle controls, we shuffled rule block's identity.

Reorientation bias

In Figure 1h,j we report reorientation magnitude as an index of temperature-induced innate turning behavior [17, 18]. This was defined as the average absolute reorientation angle of the first swim detected after $temp_{DOWN}$ for trials where the preceding ITI was lower than 7.5 sec. For shuffle controls, we randomly selected swims throughout the experiment.

Cold exposure time

In Figure 1f,k we report cold exposure time as a measure of task performance. This was defined as the average time spent from $temp_{DOWN}$ to $temp_{UP}$ for trials where the preceding ITI was lower than 7.5 sec. For delay experiments, this value was corrected by the applied delay to represent cold exposure time under a zero-delay condition.

Preprocessing of imaging data

All functional data were drift-corrected using the Python package fimpy (https://github.com/portugueslab/fimpy) or suite2p [78]. ROIs were manually extracted using napari (https://napari.org/stable/) based on clear anatomical landmarks, except for habenula somata (extracted using suite2p) and dPPR neurons (extracted using fimpy). Each ROI was resampled at 5 Hz with linearly spaced timepoints. Baseline fluorescence (F0) was defined as the median over the entire experiment. ΔF/F was computed as (F-F0)/F0, where F is the instantaneous fluorescence from the raw ROI time series. These time series were then smoothed with a third-order Savitzky–Golay filter over 11 frames.

Fraction of temperature-responding r-dHb neurons

In Figure S4c, we report the fraction of temperature-modulated r-dHb neurons. Only positive modulations (increases from baseline fluorescence) were considered. To determine this fraction, we first calculated the evoked using a 10-second window centered on stimulus onset or offset (each condition analyzed separately). Baseline activity was subtracted, and the average response was calculated. This procedure was repeated 1000 times, each time circularly shuffling the original trace to create a null distribution of evoked activity. A p-value was computed per neuron, and the fraction of responsive neurons was defined as the proportion with p-values below 0.05.

ON response dynamics

Related to Figure S4d,e,f r-dHb ON response dynamics were classified by first computing the $temp_{UP}$ triggered average. We then extracted the ΔF/F from 0–2 sec. and 8–10 sec. These values were used to calculate a polar angle describing the relative ΔF/F over the two time windows. For example, a fast-adapting neuron with a greater increase in the first window compared to the second would have a polar angle close to zero, whereas a slow-adapting neuron would have an angle close to 90 degrees. Arbitrary thresholds were then set to categorize response profiles.

Multiplication index

Related to Figure 2f, Figure 4e,i and Figure S6b,c. For iIPN and r-dHb somata imaging, we computed this index only on the subset of neurons significantly modulated by $temp_{UP}$ while for the rest of the experiments we directly computed it on the two traces of $glomerular^{iIPN/dPPR}$ or corresponding dHb axon patches. We then computed the triggered average for every choice-outcome combination and calculated the maximum ΔF/F increase over a 10-sec window. The multiplication index was then computed as the negative log-ratio between: (1) the difference in between CCW and CW swims in the absence of thermal feedback and (2) the difference in between CCW and CW swims when they led to $temp_{UP}$.

Anatomy-based choice-outcome responses

Related to Figure 2e, Figure 4d,j and Figure S9e. For every neuron we computed the triggered average for every choice-outcome combination and calculated the average ΔF/F increase over a 10 sec. window. Then, we pooled CCW (divided by outcome responses) responses for neurons located on the right brain hemisphere with CW responses for the ones located on the left hemisphere and did the same for the opposite combination. Then we computed the median across neurons within the same animal.

Sensorimotor lag

Related to Figure 2h. During open-loop stimulation, each $temp_{UP}$ instance was assigned a sensorimotor lag value. We searched for the closest swim event within a 2-second window before (-2 sec) and after (+2 sec) $temp_{UP}$. Sensorimotor lag was defined as the difference between the timing of the first swim onset and $temp_{UP}$. Trials where the sensorimotor lag was positive but the fish swam at least 5 seconds before $temp_{UP}$ were excluded. Finally, we did the same pooling criterion used for the "Anatomy-based choice-outcome responses". For Figure 2h, sensorimotor lag was binned with 0.5-sec. spacing.

F/F standard deviation analysis

Related to Figure S9c-d. Starting from the ΔF/F aligned stacks (time,y,x), we computed, for every pixel, the standard deviation over time. In this way, we obtained a bi-

dimensional map (y,x). For Figure S9c we then calculated the rigid transformation matrix (RigidTransform2D class from the python package dipy) for all the acquisitions using aligned stack sum projections in a common reference (a selected recording). Finally, we transformed all standard deviation maps and averaged across fish. For Figure S9d we then obtained, from each map, the average standard deviation value in dHb axons by averaging in space and calculated the ratio for first and second imaging session across conditions.

Pixel-wise PCA

Related to Figure 4b. Imaging experiment can be seen as a 3-dimensional matrix (t,y,x). We flattened this matrix to obtain a bi-dimensional matrix (t,y*x), selected only pixels belonging to dHb axons and not to background, and performed PCA along the y*x dimension. Then, from the PCA loadings we reconstructed the original anatomical image to generate a loading map for the first 6 PCs.

Maps generation for dPPR population imaging

Related to Figure S10. Eighteen different regressors were created to cover the sensory, motor, and sensorimotor response space:

- Responses that linearly scaled with temperature (both excitatory and inhibitory)
- Derivative responses (responding to increases and/or decreases in temperature)
- Responses excited by all swim events
- Responses related to swim vigor
- Selective responses for forward swims
- Choice-selective responses (either CCW or CW)
- Bidirectional choice-selective responses (CCW excited/CW inhibited or vice versa), similar to glomeruli^{dPPR}-like responses
- glomerulus^{iIPN} responses, responding to either to $temp_{UP}$ or $temp_{DOWN}$

For each neuron, we calculated the Pearson's correlation with each regressor and obtained a p-value by circularly shuffling the original calcium trace 500 times. Each neuron was then categorized by the regressor with the lowest p-value (and strictly below 0.05). Next, for each fish (and after brain registrations on common atlas), we computed the distance between each neuron and corresponding neurons in other fish brains within the same response category. A neuron was retained if a matching neuron within a 20 micron radius was found in at least 50% of the animals, ensuring reliable dPPR maps. Finally, we repeated this procedure separately for the left and right hemispheres: we kept neurons if a corresponding neuron in the contralateral hemisphere was present within a 10 micron radius.

Electron microscopy reconstructions

EM reconstructions were performed on an open-access Serial Blockface EM dataset from a 5 dpf larval Tg(elavl3:GCaMP5G)a4598 sampled at a resolution of 14 x 14 x 25 nm [29]. The IPN region was identified based on prior work [24, 26]. Reconstructions were generated by merging neurite segments identified by an automated flood-filling algorithm as described in [29]. The first reconstructed neurons were from the iIPN shell, traced by annotators at ariadne.ai AG, starting from seed points corresponding to iIPN shell somata selected by the authors. Each completed cell underwent a quality review by an expert annotator. From the aggregated mesh, neuron skeletons were extracted using custom python software. Presynaptic partners were identified by first detecting synapses with a detection algorithm [29], followed by manual curation of contact points (as done elsewhere [26, 79]) and tracing of partner neurons. Partner reconstruction and quality control were performed by both ariadne.ai AG and the authors. Unlike iIPN shell, reconstructing partner neurons was more challenging due to neurites extending into blurred areas of the dataset, making this reconstruction effort incomplete. Similarly, most of the dHb axons are incomplete, due to a discontinuity in the dataset in the posterior-ventral-left IPN. Left- and right-dHb afferents were distinguished by the side of the fasciculus retroflexus along which each reconstructed axon traveled. Reconstructions classification was done manually based on dendritic and axonal positioning. Cellular compartments (glomeruli and axons) were identified by morphological characteristics such as process thickness. iIPN glomeruli were classified using the DBSCAN clustering algorithm from the sklearn library in Python.

Statistics

- Figure 1d: reorientation bias CCW block: - 0.093 ± 0.037 rad., mean ± s.e.m. vs. CW block: + 0.130 ± 0.040 rad., mean ± s.e.m.; two-sided Wilcoxon signed-rank test, p<0.0001; CCW shuffle block: + 0.013 ± 0.033 rad., mean ± s.e.m. vs. CW shuffle block: + 0.121 ± 0.032 rad., mean ± s.e.m.; two-sided Wilcoxon signed-rank test, p=0.86; CCW block vs. CCW shuffle block, two-sided Wilcoxon signed-rank test, p<0.01; CW block vs. CCW shuffle block, two-sided Wilcoxon signed-rank test, p < 0.001
- Figure 1f: exposure time 0 sec. delay: + 1.985 ± 0.171 sec., mean ± s.e.m., exposure time 0.4 sec. delay: + 3.19 ± 0.388 sec., mean ± s.e.m., exposure time 0.8 sec. delay: + 3.432 ± 0.418 sec., mean ± s.e.m.. 0 delay vs. 0.4 delay, two-sided T-test, p < 0.01, 0 delay vs. 0.8 delay, two-sided T-test, p < 0.01, 0.4 delay vs. 0.8 delay, two-sided T-test, p = 0.685
- Figure 1g: reorientation bias 0 delay: + 0.231 ± 0.070 rad., mean ± s.e.m., reorientation bias 0 delay shuffle: - 0.0005 ± 0.006 rad., mean ± s.e.m., reorientation bias 0.4 delay: + 0.106 ± 0.044 rad., mean ± s.e.m., reorientation bias 0.4 delay shuffle: + 0.01 ± 0.006 rad., mean ± s.e.m., reorientation bias 0.8 delay: - 0.053 ± 0.07 rad., mean ± s.e.m., reorientation bias 0.8 delay shuffle: + 0.004 ± 0.006 rad., mean ± s.e.m.. 0 delay vs. 0 delay shuffle, two-sided Wilcoxon signed-rank test, p < 0.001, 0.4 delay vs. 0.4 delay shuffle, two-sided Wilcoxon signed-rank test, p = 0.114, 0.8 delay vs. 0.8 delay shuffle, two-sided Wilcoxon signed-rank test, p = 0.231
- Figure 1h: reorientation magnitude 0 sec. delay: +

1.159 ± 0.114 rad., mean ± s.e.m., reorientation magnitude 0 rad. delay shuffle: + 0.673 ± 0.037 rad., mean ± s.e.m., reorientation magnitude 0'.4 sec. rad: + 1.018 ± 0.112 rad., mean ± s.e.m., reorientation magnitude 0.4 rad. delay shuffle: + 0.651 ± 0.033 rad., mean ± s.e.m., reorientation magnitude 0.8 rad. delay: + 1.027 ± 0.115 rad., mean ± s.e.m., reorientation magnitude 0.8 rad. delay shuffle: + 0.699 ± 0.057 rad., mean ± s.e.m.. 0 delay vs. 0 delay shuffle, two-sided Wilcoxon signed-rank test, $p < 0.001$, 0.4 delay vs. 0.4 delay shuffle, two-sided Wilcoxon signed-rank test, $p < 0.001$, 0.8 delay vs. 0.8 delay shuffle, two-sided Wilcoxon signed-rank test, $p < 0.01$

- Figure 1j: reorientation magnitude ctrl: + 1.363 ± 0.115 rad., mean ± s.e.m., reorientation magnitude ctrl shuffle: + 0.715 ± 0.044 rad., mean ± s.e.m., reorientation magnitude ablation: + 1.345 ± 0.129 rad., mean ± s.e.m., reorientation magnitude ablation: + 0.844 ± 0.122 rad., mean ± s.e.m.. ctrl vs. ctrl shuffle, two-sided Wilcoxon signed-rank test, $p < 0.001$, ablation vs. ablation shuffle, two-sided Wilcoxon signed-rank test, $p < 0.01$
- Figure 1k: exposure time ctrl: + 2.355 ± 0.147 sec., mean ± s.e.m., exposure time ablation: + 3.069 ± 0.270 sec., mean ± s.e.m., exposure time 0.8 sec. delay: + 3.432 ± 0.418 sec., mean ± s.e.m.. ctrl vs. ablation, two-sided T-test, $p < 0.05$
- Figure 1l: reorientation bias ctrl: + 0.127 ± 0.05 rad., mean ± s.e.m., reorientation bias ctrl shuffle: + 0.002 ± 0.006 rad., mean ± s.e.m., reorientation bias ablation: + 0.030 ± 0.061 rad., mean ± s.e.m., reorientation bias ablation shuffle: + 0.030 ± 0.061 rad., mean ± s.e.m.. ctrl vs. ctrl shuffle, two-sided Wilcoxon signed-rank test, $p<0.01$, ablation vs. ablation shuffle, two-sided Wilcoxon signed-rank test, $p = 0.397$
- Figure 2e: pref. reor. + no change: 0.04, median, pref. reor. + $temp_{UP}$: 0.288, median, pref. reor. + $temp_{DOWN}$: -0.051, median, fwd + no change: -0.04, median, fwd + $temp_{UP}$: 0.164, median, fwd + $temp_{DOWN}$: -0.073, opp. reor. + no change: -0.009, median, opp. reor. + $temp_{UP}$: 0.099, opp. reor. + $temp_{DOWN}$: -0.008, pref. reor. + no change vs. opp. reor. + no change, two-sided Wilcoxon signed-rank test, $p < 0.001$, pref. reor. + $temp_{UP}$ vs. opp. reor. + $temp_{UP}$, two-sided Wilcoxon signed-rank test, $p < 0.001$, pref. reor. + no change vs. pref. reor. + $temp_{UP}$, two-sided Wilcoxon signed-rank test, $p < 0.001$
- Figure 2f: MI $glomerulus^{iIPN}$: 1.413, median, two-sided Wilcoxon signed-rank test, $p < 0.001$
- Figure 2h: ΔF/F glom. pref. reor. (from left to right): 0.034, 0.056, 0.079, 0.184, 0.0156, 0.0452, 0.0714, 0.063, mean. ΔF/F glom. opp. reor. (from left to right): 0.041, 0.08, 0.0816, 0.076, 0.033, 0.067, 0.093, 0.0761, mean. ΔF/F glom. pref. reor. [-0.5,0] vs, ΔF/F glom. pref. reor. [0,0.5], two-sided Mann-Whitney U test, $p < 0.05$
- Figure 2i: ΔF/F only motor: + 0.068 ± 0.013, mean ± s.e.m., ΔF/F only sensory: + 0.289 ± 0.048, mean ± s.e.m., ΔF/F sensory + motor (arithmetic sum): + 0.358 ± 0.053, mean ± s.e.m., ΔF/F sensory + motor (observed): + 0.563 ± 0.098, mean ± s.e.m.. ΔF/F sensory + motor (arithmetic sum) vs. ΔF/F sensory + motor (observed), two-sided Wilcoxon signed-rank test, $p < 0.01$
- Figure 4d: pref. reor. + no change: 0.014, median, pref. reor. + $temp_{UP}$: 0.095, median, pref. reor. + $temp_{DOWN}$: 0.019, median, fwd + no change: 0.002, median, fwd + $temp_{UP}$: 0.022, median, fwd + $temp_{DOWN}$: 0.009, opp. reor. + no change: -0.026, median, opp. reor. + $temp_{UP}$: 0, opp. reor. + $temp_{DOWN}$: -0.04, pref. reor. + no change vs. opp. reor. + no change, two-sided Wilcoxon signed-rank test, $p < 0.05$, pref. reor. + $temp_{UP}$ vs. opp. reor. + $temp_{UP}$, two-sided Wilcoxon signed-rank test, $p < 0.05$, pref. reor. + no change vs. pref. reor. + $temp_{UP}$, two-sided Wilcoxon signed-rank test, $p < 0.05$.
- Figure 4e: MI $glomerulus^{dHb}$: 0.366, median, two-sided Wilcoxon signed-rank test, $p < 0.01$
- Figure 4g: lateral glomerulus (pref. reor. + $temp_{UP}$): pre ctrl vs. post ctrl: two-sided Wilcoxon signed-rank test, $p = 0.425$. pre treatment vs. post treatment: two-sided Wilcoxon signed-rank test, $p < 0.05$. medial glomerulus (pref. reor. + $temp_{DOWN}$): pre ctrl vs. post ctrl: two-sided Wilcoxon signed-rank test, $p = 0.937$. pre treatment vs. post treatment: two-sided Wilcoxon signed-rank test, $p = 0.570$.
- Figure 4i: MI $glomerulus^{dPPR}$ ($temp_{UP}$): 0.072, median, two-sided Wilcoxon signed-rank test, $p = 0.376$. MI $glomerulus^{dPPR}$ ($temp_{DOWN}$): 0.014, median, two-sided Wilcoxon signed-rank test, $p = 0.909$.
- Figure 4j: pref. reor. + no change: 0.054, median, pref. reor. + $temp_{UP}$: 0.063, median, pref. reor. + $temp_{DOWN}$: 0.016, median, fwd + no change: 0.015, median, fwd + $temp_{UP}$: 0.025, median, fwd + $temp_{DOWN}$: - 0.082, opp. reor. + no change: -0.063, median, opp. reor. + $temp_{UP}$: -0.015, opp. reor. + $temp_{DOWN}$: -0.073, pref. reor. + no change vs. opp. reor. + no change, two-sided Wilcoxon signed-rank test, $p < 0.05$, pref. reor. + $temp_{UP}$ vs. opp. reor. + $temp_{UP}$, two-sided Wilcoxon signed-rank test, $p < 0.01$, pref. reor. + no change vs. pref. reor. + $temp_{UP}$, two-sided Wilcoxon signed-rank test, $p = 0.684$.
- Figure S1f: thermal choice ROI occupancy: + 67.593 %, median vs. ctrl: + 24.321 %, median; two-sided Mann-Whitney U test, $p < 0.01$
- Figure S1g: outside ROI exposure time: + 0.68 sec., median vs. ctrl: + 32.325 sec., median, two-sided Mann-Whitney U test, $p < 0.05$
- Figure S1h: ROI occupancy first half: + 68.205 %, median vs. second half: + 67.515 %, median, two-sided Wilcoxon signed-rank test, $p = 0.393$
- Figure S2c: Angular velocity CCW block: - 0.261 rad./sec., median vs. Angular velocity CW block: + 0.303 rad./sec., median, two-sided Wilcoxon signed-rank test, $p < 0.001$
- Figure S2e: reorientation bias ITI CCW block: - 0.011 ± 0.010 rad., mean ± s.e.m., Reorientation bias ITI CW block: - 0.016 ± 0.008 rad. two-sided Wilcoxon signed-rank test, $p = 0.633$
- Figure S2f: reorientation bias short ITIs: + 0.07 ± 0.029 rad., mean ± s.e.m. vs. reorientation bias shuffle short ITIs: + 0.0007 ± 0.028 rad., mean ± s.e.m.. reorientation bias long ITIs: + 0.0002 ± 0.053 rad., mean ± s.e.m., reorientation bias shuffle long ITIs:

- 0.003 ± 0.004 rad., mean ± s.e.m.. reorientation bias short ITIs vs. reorientation bias shuffle short ITIs, two-sided Wilcoxon signed-rank test, p<0.05, reorientation bias long ITIs vs. reorientation bias shuffle long ITIs, two-sided Wilcoxon signed-rank test, p = 0.98
- Figure S2h: reaction time 0 delay: + 0.903 ± 0.026 sec., mean ± s.e.m., reaction time 0.4 delay: + 0.999 ± 0.026 sec., mean ± s.e.m., reaction time 0.8 delay: + 1.014 ± 0.033 sec., mean ± s.e.m.. 0 delay vs. 0.4 delay, two-sided T-test, p < 0.05, 0 delay vs. 0.8 delay, two-sided T-test, p < 0.01, 0.4 delay vs. 0.8 delay, two-sided T-test, p = 0.771
- Figure S2j: reaction time ctrl: + 0.908 ± 0.028 sec., mean ± s.e.m., reaction time ablation: + 0.980 ± 0.029 sec., mean ± s.e.m.. ctrl vs. ablation, two-sided T-test, p = 0.073
- Figure S2k: swim rate control group: + 0.844 ± 0.027 swim/sec.; swim rate ablation group: + 0.822 ± 0.027 swim/sec., mean ± s.e.m.; two-sided T-test, p = 0.562
- Figure S2l: inter-swim interval control group: + 0.898 ± 0.021 sec.; inter-swim interval ablation group: + 0.940 ± 0.021 sec., mean ± s.e.m.; two-sided T-test, p = 0.164
- Figure S2m: distance traveled during swim control group: + 1.972 ± 0.047 mm.; distance traveled during swim ablation group: + 2.001 ± 0.049 swim/sec., mean ± s.e.m.; two-sided T-test, p = 0.668
- Figure S2n: swim duration control group: + 0.264 ± 0.007 sec.; swim duration ablation group: + 0.264 ± 0.007 swim/sec., mean ± s.e.m.; two-sided T-test, p = 0.932
- Figure S4c: ON fraction: + 34.5 %, median, OFF fraction: + 16.9 %, median. ON fraction vs. OFF fraction, two-sided Wilcoxon signed-rank test, p < 0.05
- Figure S6b: MI r-dHb: 0.26, median, MI iIPN: 1.08, median; r-dHb vs. iIPN, two-sided Mann-Whitney U test, p < 0.001
- Figure S6c: Bonferroni corrected two-sided Mann-Whitney U test, p < 0.05
- Figure S6e: ΔF/F temp. incr. ctrl: 0.44, median, ΔF/F temp. incr. ablation: 0.16, median; ctrl vs. ablation, two-sided Mann-Whitney U test, p < 0.001
- Figure S8d: neurons count $dPPR^{ipsi}$: 24, median, neurons count $dPPR^{contra}$: 29, median, two-sided Wilcoxon signed-rank test, p = 0.25
- Figure S9b: ctrl: two-sided Wilcoxon signed-rank test, p = 0.570. treatment: two-sided Wilcoxon signed-rank test, p = 0.296
- Figure S9d: ctrl vs. treatment: two-sided Mann-Whitney U test, p < 0.299
- Figure S9i: pref.reor.+no change vs. pref.reor.+ $temp_{UP}$: two-sided Wilcoxon signed-rank test, p = 0.685. pref.reor.+no change vs. pref.reor.+ $temp_{DOWN}$: two-sided Wilcoxon signed-rank test, p = 0.376.

Data and code availability

All the data described in the paper, the analysis notebooks and the figure generation notebooks will be made available upon publication.

References

1. Minsky, M. Steps toward Artificial Intelligence. *Proc. IRE* **49,** 8–30. ISSN: 0096-8390. doi:10.1109/JRPROC.1961.287775 (Jan. 1961).
2. Parker, N. F. *et al.* Reward and choice encoding in terminals of midbrain dopamine neurons depends on striatal target. *Nat Neurosci* **19,** 845–854. ISSN: 1097-6256, 1546-1726. doi:10.1038/nn.4287 (June 2016).
3. Bloem, B. *et al.* Multiplexed action-outcome representation by striatal striosome-matrix compartments detected with a mouse cost-benefit foraging task. *Nat Commun* **13,** 1541. ISSN: 2041-1723. doi:10.1038/s41467-022-28983-5 (Mar. 22, 2022).
4. Locantore, J. R. *et al. Mixed representations of choice direction and outcome by GABA/glutamate cotransmitting neurons in the entopeduncular nucleus* Jan. 6, 2025. doi:10.7554/eLife.100488.2.
5. Hayden, B. Y. & Platt, M. L. Neurons in Anterior Cingulate Cortex Multiplex Information about Reward and Action. *J. Neurosci.* **30,** 3339–3346. ISSN: 0270-6474, 1529-2401. doi:10.1523/JNEUROSCI.4874-09.2010 (Mar. 3, 2010).
6. Witkowski, P. P. *et al. Neural mechanisms of credit assignment for delayed outcomes during contingent learning* Oct. 9, 2024. doi:10.7554/eLife.101841.1.
7. Rozin, P. N. & Mayer, J. Thermal Reinforcement and Thermoregulatory Behavior in the Goldfish, *Carassius auratus*. *Science* **134,** 942–943. ISSN: 0036-8075, 1095-9203. doi:10.1126/science.134.3483.942 (Sept. 29, 1961).
8. Neill, W. H., Magnuson, J. J. & Chipman, G. G. Behavioral Thermoregulation by Fishes: A New Experimental Approach. *Science* **176,** 1443–1445. ISSN: 0036-8075, 1095-9203. doi:10.1126/science.176.4042.1443 (June 30, 1972).
9. Schulze, G., Tetzner, M. & Topolinski, H. Operant thermoregulation of rats with anterior hypothalamic lesions. *Naunyn-Schmiedeberg's Arch. Pharmacol.* **318,** 43–48. ISSN: 0028-1298, 1432-1912. doi:10.1007/BF00503311 (Dec. 1981).
10. Lin, Q. *et al.* Cerebellar Neurodynamics Predict Decision Timing and Outcome on the Single-Trial Level. *Cell* **180,** 536–551.e17. ISSN: 00928674. doi:10.1016/j.cell.2019.12.018 (Feb. 2020).
11. Jung, S. *et al.* A forebrain neural substrate for behavioral thermoregulation. *Neuron* **110,** 266–279.e9. ISSN: 08966273. doi:10.1016/j.neuron.2021.09.039 (Jan. 2022).
12. Kemp, F. D. Thermal reinforcement and thermoregulatory behaviour in the lizard Dipsosaurus dorsalis: An operant technique. *Animal Behaviour* **17,** 446–451. ISSN: 00033472. doi:10.1016/0003-3472(69)90145-6 (Aug. 1969).
13. Chen, X.-M. *et al.* New apparatus for studying behavioral thermoregulation in rats. *Physiology & Behavior* **64,** 419–424. ISSN: 00319384. doi:10.1016/S0031-9384(98)00094-8 (June 1998).
14. Aizawa, H., Amo, R. & Okamoto, H. Phylogeny and Ontogeny of the Habenular Structure. *Front. Neurosci.* **5.** ISSN: 1662-4548. doi:10.3389/fnins.2011.00138 (2011).
15. Okamoto, H., Cherng, B.-W., Nakajo, H., Chou, M.-Y. & Kinoshita, M. Habenula as the experience-dependent controlling switchboard of behavior and attention in social conflict and learning. *Current Opinion in Neurobiology* **68,** 36–43. ISSN: 09594388. doi:10.1016/j.conb.2020.12.005 (June 2021).

16. Haesemeyer, M., Robson, D., Li, J., Schier, A. & Engert, F. The Structure and Timescales of Heat Perception in Larval Zebrafish. *Cell Systems* **1,** 338–348. ISSN: 24054712. doi:10.1016/j.cels.2015.10.010 (Nov. 2015).

17. Palieri, V. *et al.* The preoptic area and dorsal habenula jointly support homeostatic navigation in larval zebrafish. *Current Biology* **34,** 489–504.e7. ISSN: 09609822. doi:10.1016/j.cub.2023.12.030 (Feb. 2024).

18. Haesemeyer, M., Robson, D. N., Li, J. M., Schier, A. F. & Engert, F. A Brain-wide Circuit Model of Heat-Evoked Swimming Behavior in Larval Zebrafish. *Neuron* **98,** 817–831.e6. ISSN: 08966273. doi:10.1016/j.neuron.2018.04.013 (May 2018).

19. Lovett-Barron, M. *et al.* Multiple convergent hypothalamus–brainstem circuits drive defensive behavior. *Nat Neurosci* **23,** 959–967. ISSN: 1097-6256, 1546-1726. doi:10.1038/s41593-020-0655-1 (Aug. 2020).

20. Duboué, E. R., Hong, E., Eldred, K. C. & Halpern, M. E. Left Habenular Activity Attenuates Fear Responses in Larval Zebrafish. *Current Biology* **27,** 2154–2162.e3. ISSN: 09609822. doi:10.1016/j.cub.2017.06.017 (July 2017).

21. Agetsuma, M. *et al.* The habenula is crucial for experience-dependent modification of fear responses in zebrafish. *Nat Neurosci* **13,** 1354–1356. ISSN: 1097-6256, 1546-1726. doi:10.1038/nn.2654 (Nov. 2010).

22. Palumbo, F., Serneels, B., Pelgrims, R. & Yaksi, E. The Zebrafish Dorsolateral Habenula Is Required for Updating Learned Behaviors. *Cell Reports* **32,** 108054. ISSN: 22111247. doi:10.1016/j.celrep.2020.108054 (Aug. 2020).

23. Lee, A. *et al.* The Habenula Prevents Helpless Behavior in Larval Zebrafish. *Current Biology* **20,** 2211–2216. ISSN: 09609822. doi:10.1016/j.cub.2010.11.025 (Dec. 2010).

24. Petrucco, L. *et al.* Neural dynamics and architecture of the heading direction circuit in zebrafish. *Nat Neurosci* **26,** 765–773. ISSN: 1097-6256, 1546-1726. doi:10.1038/s41593-023-01308-5 (May 2023).

25. Markov, D. A., Petrucco, L., Kist, A. M. & Portugues, R. A cerebellar internal model calibrates a feedback controller involved in sensorimotor control. *Nat Commun* **12,** 6694. ISSN: 2041-1723. doi:10.1038/s41467-021-26988-0 (Nov. 18, 2021).

26. Wu, Y. K., Petrucco, L. & Portugues, R. *Anatomical and functional organization of the interpeduncular nucleus in larval zebrafish* Oct. 12, 2024. doi:10.1101/2024.10.09.617353.

27. Scott, E. K. The cellular architecture of the larval zebrafish tectum, as revealed by Gal4 enhancer trap lines. *Front. Neural Circuits* **3.** ISSN: 16625110. doi:10.3389/neuro.04.013.2009 (2009).

28. Lavian, H., Prat, O., Petrucco, L., Štih, V. & Portugues, R. *The representation of visual motion and landmark position aligns with heading direction in the zebrafish interpeduncular nucleus* Sept. 27, 2024. doi:10.1101/2024.09.25.614953.

29. Svara, F. *et al.* Automated synapse-level reconstruction of neural circuits in the larval zebrafish brain. *Nat Methods* **19,** 1357–1366. ISSN: 1548-7091, 1548-7105. doi:10.1038/s41592-022-01621-0 (Nov. 2022).

30. Bianco, I. *et al.* The Tangential Nucleus Controls a Gravito-inertial Vestibulo-ocular Reflex. *Current Biology* **22,** 1285–1295. ISSN: 09609822. doi:10.1016/j.cub.2012.05.026 (July 2012).

31. Dragomir, E. I., Štih, V. & Portugues, R. Evidence accumulation during a sensorimotor decision task revealed by whole-brain imaging. *Nat Neurosci* **23,** 85–93. ISSN: 1097-6256, 1546-1726. doi:10.1038/s41593-019-0535-8 (Jan. 2020).

32. Bianco, I. H. & Wilson, S. W. The habenular nuclei: a conserved asymmetric relay station in the vertebrate brain. *Phil. Trans. R. Soc. B* **364,** 1005–1020. ISSN: 0962-8436, 1471-2970. doi:10.1098/rstb.2008.0213 (Apr. 12, 2009).

33. Zaupa, M. *et al.* Trans-inhibition of axon terminals underlies competition in the habenulo-interpeduncular pathway. *Current Biology* **31,** 4762–4772.e5. ISSN: 09609822. doi:10.1016/j.cub.2021.08.051 (Nov. 2021).

34. Zhang, J. *et al.* Presynaptic Excitation via GABA B Receptors in Habenula Cholinergic Neurons Regulates Fear Memory Expression. *Cell* **166,** 716–728. ISSN: 00928674. doi:10.1016/j.cell.2016.06.026 (July 2016).

35. Koppensteiner, P. *et al.* GABA $_B$ receptors induce phasic release from medial habenula terminals through activity-dependent recruitment of release-ready vesicles. *Proc. Natl. Acad. Sci. U.S.A.* **121,** e2301449121. ISSN: 0027-8424, 1091-6490. doi:10.1073/pnas.2301449121 (Feb. 20, 2024).

36. Stinson, H. E. & Ninan, I. *GABA$_B$ receptor-mediated potentiation of ventral medial habenula glutamatergic transmission in GABAergic and glutamatergic interpeduncular nucleus neurons* Jan. 3, 2025. doi:10.1101/2025.01.03.631193.

37. Morrison, S. F., Sved, A. F. & Passerin, A. M. GABA-mediated inhibition of raphe pallidus neurons regulates sympathetic outflow to brown adipose tissue. *American Journal of Physiology-Regulatory, Integrative and Comparative Physiology* **276,** R290–R297. ISSN: 0363-6119, 1522-1490. doi:10.1152/ajpregu.1999.276.2.R290 (Feb. 1, 1999).

38. Anderson, L. S., Costabile, J. D., Schwinn, S., Calderon, D. & Haesemeyer, M. *Sensorimotor integration enhances temperature stimulus processing* Oct. 18, 2024. doi:10.1101/2024.10.15.618474.

39. Thompson, R. Interpeduncular Nucleus and Avoidance Conditioning in the Rat. *Science* **132,** 1551–1553. ISSN: 0036-8075, 1095-9203. doi:10.1126/science.132.3439.1551 (Nov. 25, 1960).

40. Liang, J. *et al.* A brainstem circuit amplifies aversion. *Neuron,* S0896627324005828. ISSN: 08966273. doi:10.1016/j.neuron.2024.08.010 (Sept. 2024).

41. Cherng, B.-W., Islam, T., Torigoe, M., Tsuboi, T. & Okamoto, H. The Dorsal Lateral Habenula-Interpeduncular Nucleus Pathway Is Essential for Left-Right-Dependent Decision Making in Zebrafish. *Cell Reports* **32,** 108143. ISSN: 22111247. doi:10.1016/j.celrep.2020.108143 (Sept. 2020).

42. Dreosti, E., Vendrell Llopis, N., Carl, M., Yaksi, E. & Wilson, S. Left-Right Asymmetry Is Required for the Habenulae to Respond to Both Visual and Olfactory Stimuli. *Current Biology* **24,** 440–445. ISSN: 09609822. doi:10.1016/j.cub.2014.01.016 (Feb. 2014).

43. Koide, T., Yabuki, Y. & Yoshihara, Y. Terminal Nerve GnRH3 Neurons Mediate Slow Avoidance of Carbon Dioxide in Larval Zebrafish. *Cell Reports* **22,** 1115–1123. ISSN: 22111247. doi:10.1016/j.celrep.2018.01.019 (Jan. 2018).

44. Herrera, K. J., Panier, T., Guggiana-Nilo, D. & Engert, F. Larval Zebrafish Use Olfactory Detection of Sodium and Chloride to Avoid Salt Water. *Current Biology* **31,** 782–793.e3. ISSN: 09609822. doi:10.1016/j.cub.2020.11.051 (Feb. 2021).

45. Aizawa, H. *et al.* Laterotopic Representation of Left-Right Information onto the Dorso-Ventral Axis of a Zebrafish Midbrain Target Nucleus. *Current Biology* **15,** 238–243. ISSN: 09609822. doi:10.1016/j.cub.2005.01.014 (Feb. 2005).

46. Bianco, I. H., Carl, M., Russell, C., Clarke, J. D. & Wilson, S. W. Brain asymmetry is encoded at the level of axon terminal morphology. *Neural Dev* **3,** 9. ISSN: 1749-8104. doi:10.1186/1749-8104-3-9 (Dec. 2008).

47. Miyasaka, N. *et al.* Olfactory projectome in the zebrafish forebrain revealed by genetic single-neuron labelling. *Nat Commun* **5,** 3639. ISSN: 2041-1723. doi:10.1038/ncomms4639 (Apr. 9, 2014).

48. Costabile, J. D., Balakrishnan, K. A., Schwinn, S. & Haesemeyer, M. Model discovery to link neural activity to behavioral tasks. *eLife* **12,** e83289. ISSN: 2050-084X. doi:10.7554/eLife.83289 (June 6, 2023).

49. Kludt, E., Okom, C., Brinkmann, A. & Schild, D. Integrating Temperature with Odor Processing in the Olfactory Bulb. *J. Neurosci.* **35,** 7892–7902. ISSN: 0270-6474, 1529-2401. doi:10.1523/JNEUROSCI.0571-15.2015 (May 20, 2015).

50. Schmid, A., Pyrski, M., Biel, M., Leinders-Zufall, T. & Zufall, F. Grueneberg Ganglion Neurons Are Finely Tuned Cold Sensors. *J. Neurosci.* **30,** 7563–7568. ISSN: 0270-6474, 1529-2401. doi:10.1523/JNEUROSCI.0608-10.2010 (June 2, 2010).

51. Fleischer, J. The Grueneberg ganglion: signal transduction and coding in an olfactory and thermosensory organ involved in the detection of alarm pheromones and predator-secreted kairomones. *Cell Tissue Res* **383,** 535–548. ISSN: 0302-766X, 1432-0878. doi:10.1007/s00441-020-03380-w (Jan. 2021).

52. Lenn, N. J. Synapses in the interpeduncular nucleus: Electron microscopy of normal and habenula lesioned rats. *J of Comparative Neurology* **166,** 73–99. ISSN: 0021-9967, 1096-9861. doi:10.1002/cne.901660106 (Mar. 1976).

53. Kinoshita, M. & Okamoto, H. Acetylcholine potentiates glutamate transmission from the habenula to the interpeduncular nucleus in losers of social conflict. *Current Biology* **33,** 2121–2135.e4. ISSN: 09609822. doi:10.1016/j.cub.2023.03.087 (June 2023).

54. Spikol, E. D., Cheng, J., Macurak, M., Subedi, A. & Halpern, M. E. Genetically defined nucleus incertus neurons differ in connectivity and function. *eLife* **12,** RP89516. ISSN: 2050-084X. doi:10.7554/eLife.89516 (May 31, 2024).

55. Iwahori, N., Nakamura, K., Kameda, S. & Tahara, H. Terminal patterns of the tegmental afferents in the interpeduncular nucleus: a Golgi study in the mouse. *Anat Embryol* **188.** ISSN: 0340-2061, 1432-0568. doi:10.1007/BF00187015 (Dec. 1993).

56. Dunn, T. W. *et al.* Brain-wide mapping of neural activity controlling zebrafish exploratory locomotion. *eLife* **5,** e12741. ISSN: 2050-084X. doi:10.7554/eLife.12741 (Mar. 22, 2016).

57. Chen, X. *et al.* Brain-wide Organization of Neuronal Activity and Convergent Sensorimotor Transformations in Larval Zebrafish. *Neuron* **100,** 876–890.e5. ISSN: 08966273. doi:10.1016/j.neuron.2018.09.042 (Nov. 2018).

58. Naumann, E. A. *et al.* From Whole-Brain Data to Functional Circuit Models: The Zebrafish Optomotor Response. *Cell* **167,** 947–960.e20. ISSN: 00928674. doi:10.1016/j.cell.2016.10.019 (Nov. 2016).

59. Bahl, A. & Engert, F. Neural circuits for evidence accumulation and decision making in larval zebrafish. *Nat Neurosci* **23,** 94–102. ISSN: 1097-6256, 1546-1726. doi:10.1038/s41593-019-0534-9 (Jan. 2020).

60. Wolf, S. *et al.* Sensorimotor computation underlying phototaxis in zebrafish. *Nat Commun* **8,** 651. ISSN: 2041-1723. doi:10.1038/s41467-017-00310-3 (Sept. 21, 2017).

61. Kawashima, T. *et al. Voltage imaging reveals circuit computations in the raphe underlying serotonin-mediated motor vigor learning* Sept. 16, 2024. doi:10.1101/2024.09.15.613083.

62. Melani, R., Von Itter, R., Jing, D., Koppensteiner, P. & Ninan, I. Opposing effects of an atypical glycinergic and substance P transmission on interpeduncular nucleus plasticity. *Neuropsychopharmacol.* **44,** 1828–1836. ISSN: 0893-133X, 1740-634X. doi:10.1038/s41386-019-0396-6 (Sept. 2019).

63. Ables, J. L. *et al.* Retrograde inhibition by a specific subset of interpeduncular α5 nicotinic neurons regulates nicotine preference. *Proc. Natl. Acad. Sci. U.S.A.* **114,** 13012–13017. ISSN: 0027-8424, 1091-6490. doi:10.1073/pnas.1717506114 (Dec. 5, 2017).

64. Sakaba, T. & Neher, E. Direct modulation of synaptic vesicle priming by GABAB receptor activation at a glutamatergic synapse. *Nature* **424,** 775–778. ISSN: 0028-0836, 1476-4687. doi:10.1038/nature01859 (Aug. 2003).

65. Chalifoux, J. R. & Carter, A. G. GABA $_B$ Receptor Modulation of Voltage-Sensitive Calcium Channels in Spines and Dendrites. *J. Neurosci.* **31,** 4221–4232. ISSN: 0270-6474, 1529-2401. doi:10.1523/JNEUROSCI.4561-10.2011 (Mar. 16, 2011).

66. Alten, B., Guzikowski, N. J., Zurawski, Z., Hamm, H. E. & Kavalali, E. T. Presynaptic mechanisms underlying GABAB-receptor-mediated inhibition of spontaneous neurotransmitter release. *Cell Reports* **38,** 110255. ISSN: 22111247. doi:10.1016/j.celrep.2021.110255 (Jan. 2022).

67. Zhang, B.-b., Yao, Y.-y., Zhang, H.-f., Kawakami, K. & Du, J.-l. Left Habenula Mediates Light-Preference Behavior in Zebrafish via an Asymmetrical Visual Pathway. *Neuron* **93,** 914–928.e4. ISSN: 08966273. doi:10.1016/j.neuron.2017.01.011 (Feb. 2017).

68. Thiele, T., Donovan, J. & Baier, H. Descending Control of Swim Posture by a Midbrain Nucleus in Zebrafish. *Neuron* **83,** 679–691. ISSN: 08966273. doi:10.1016/j.neuron.2014.04.018 (Aug. 2014).

69. Kim, D. H. *et al.* Pan-neuronal calcium imaging with cellular resolution in freely swimming zebrafish. *Nat Methods* **14,** 1107–1114. ISSN: 1548-7091, 1548-7105. doi:10.1038/nmeth.4429 (Nov. 2017).

70. Freeman, J. *et al.* Mapping brain activity at scale with cluster computing. *Nat Methods* **11,** 941–950. ISSN: 1548-7091, 1548-7105. doi:10.1038/nmeth.3041 (Sept. 2014).

71. Förster, D. *et al.* Genetic targeting and anatomical registration of neuronal populations in the zebrafish brain with a new set of BAC transgenic tools. *Sci Rep* **7,** 5230. ISSN: 2045-2322. doi:10.1038/s41598-017-04657-x (July 12, 2017).

72. Filosa, A., Barker, A., Dal Maschio, M. & Baier, H. Feeding State Modulates Behavioral Choice and Processing of Prey Stimuli in the Zebrafish Tectum. *Neuron* **90,** 596–608. ISSN: 08966273. doi:10.1016/j.neuron.2016.03.014 (May 2016).

73. Štih, V., Petrucco, L., Kist, A. M. & Portugues, R. Stytra: An open-source, integrated system for stimulation, tracking and closed-loop behavioral experiments. *PLoS Comput Biol* **15** (ed Battaglia, F. P.) e1006699. ISSN: 1553-7358. doi:10.1371/journal.pcbi.1006699 (Apr. 8, 2019).

74. Chen, X. & Engert, F. Navigational strategies underlying phototaxis in larval zebrafish. *Front. Syst. Neurosci.* **8.** ISSN: 1662-5137. doi:10.3389/fnsys.2014.00039 (Mar. 25, 2014).

75. Bergemann, D. *et al.* Nifurpirinol: A more potent and reliable substrate compared to metronidazole for nitroreductase-mediated cell ablations. *Wound Repair Regeneration* **26,** 238–244. ISSN: 1067-1927, 1524-475X. doi:10.1111/wrr.12633 (Mar. 2018).

76. Kunst, M. *et al.* A Cellular-Resolution Atlas of the Larval Zebrafish Brain. *Neuron* **103,** 21–38.e5. ISSN: 08966273. doi:10.1016/j.neuron.2019.04.034 (July 2019).

77. Huang, K.-H., Ahrens, M., Dunn, T. & Engert, F. Spinal Projection Neurons Control Turning Behaviors in Zebrafish. *Current Biology* **23,** 1566–1573. ISSN: 09609822. doi:10.1016/j.cub.2013.06.044 (Aug. 2013).

78. Pachitariu, M. *et al. Suite2p: beyond 10,000 neurons with standard two-photon microscopy* June 30, 2016. doi:10.1101/061507.

79. Dowell, C. K., Hawkins, T. & Bianco, I. H. Subsets of extraocular motoneurons produce kinematically distinct saccades during hunting and exploration. *Current Biology* **35,** 554–573.e6. ISSN: 09609822. doi:10.1016/j.cub.2024.12.010 (Feb. 2025).

Supplementary figures

Eleven supplementary supplementary figures follow.

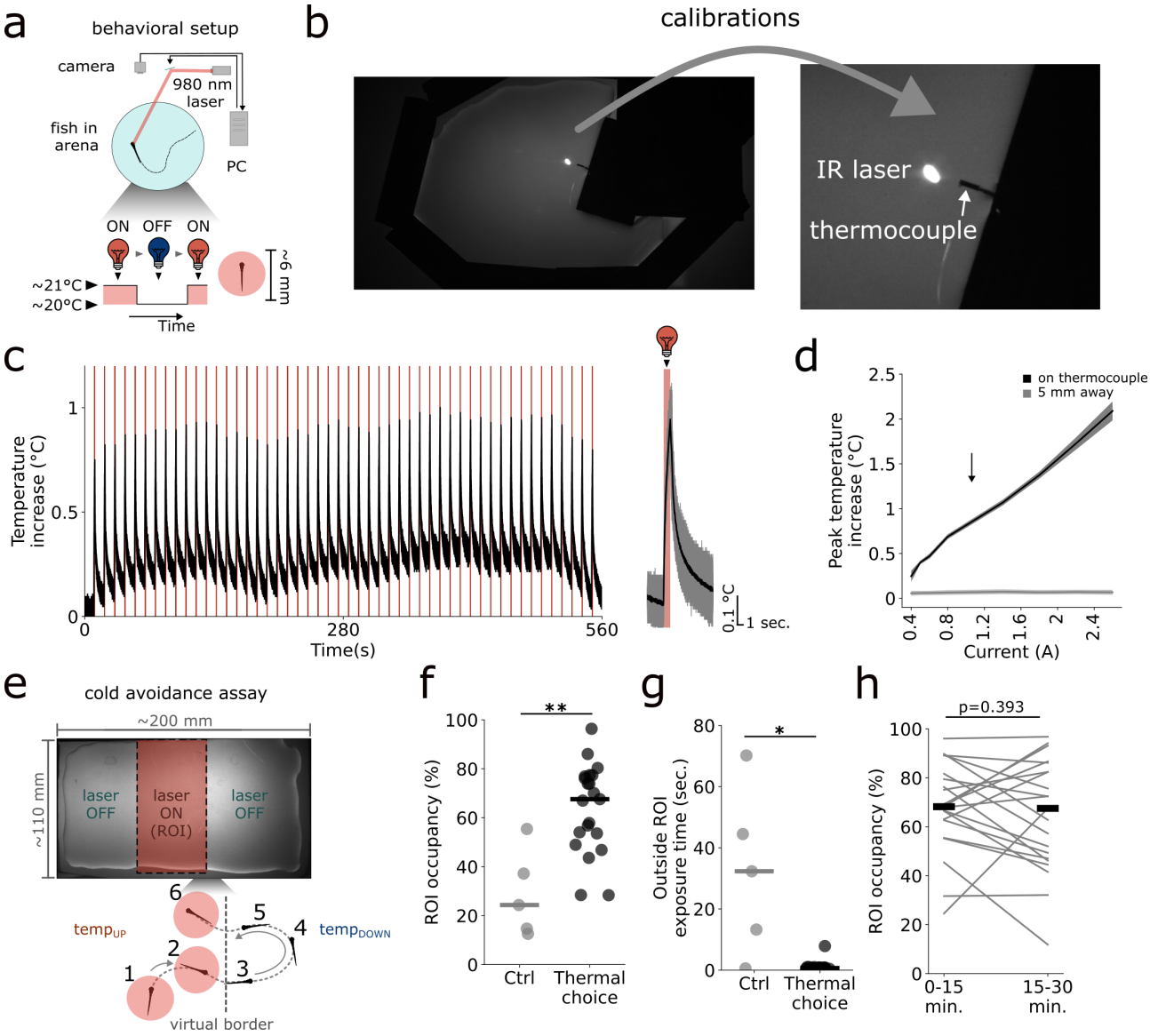

Figure S1: ***Cold avoidance with a laser-based setup.*** ***(a)*** *I: Behavioral setup used for freely swimming experiments.* ***(b)*** *Image of the IR laser and the thermocouple during calibrations.* ***(c)*** *Left: example temperature recording during a calibration session. IR laser was directed to the thermocouple for 1 second, with 10 seconds interval. Right: stimulation triggered average. In black, average temperature increases and in gray single calibration trials. In red, $temp_{UP}$ period.* ***(d)*** *Calibration curve (mean ± s.e.m.). Laser power was selected based on these results (black arrow). Black: temperature increase recorded when the IR beam was directed on the sensor. Gray: temperature increase recorded when the IR beam was directed 5 millimeters away from the sensor.* ***(e)*** *Cold avoidance assay. Fish body temperature depends on its position in the arena. Within the ROI (a rectangular region at the center), the animal experiences a warmer temperature.* ***(f)*** *ROI occupancy in control (gray) and experimental condition (black). Each dot represent the performance of a single fish, the horizontal bar the median across animals.* ***(g)*** *Median time spent outside the ROI at each exit. Each dot represent the performance of a single fish, the horizontal bar the median across animals.* ***(h)*** *ROI occupancy during the first and second halves of the 30-minute experiment. Each line represents the performance of a single fish, the horizontal bar the median across animals.*

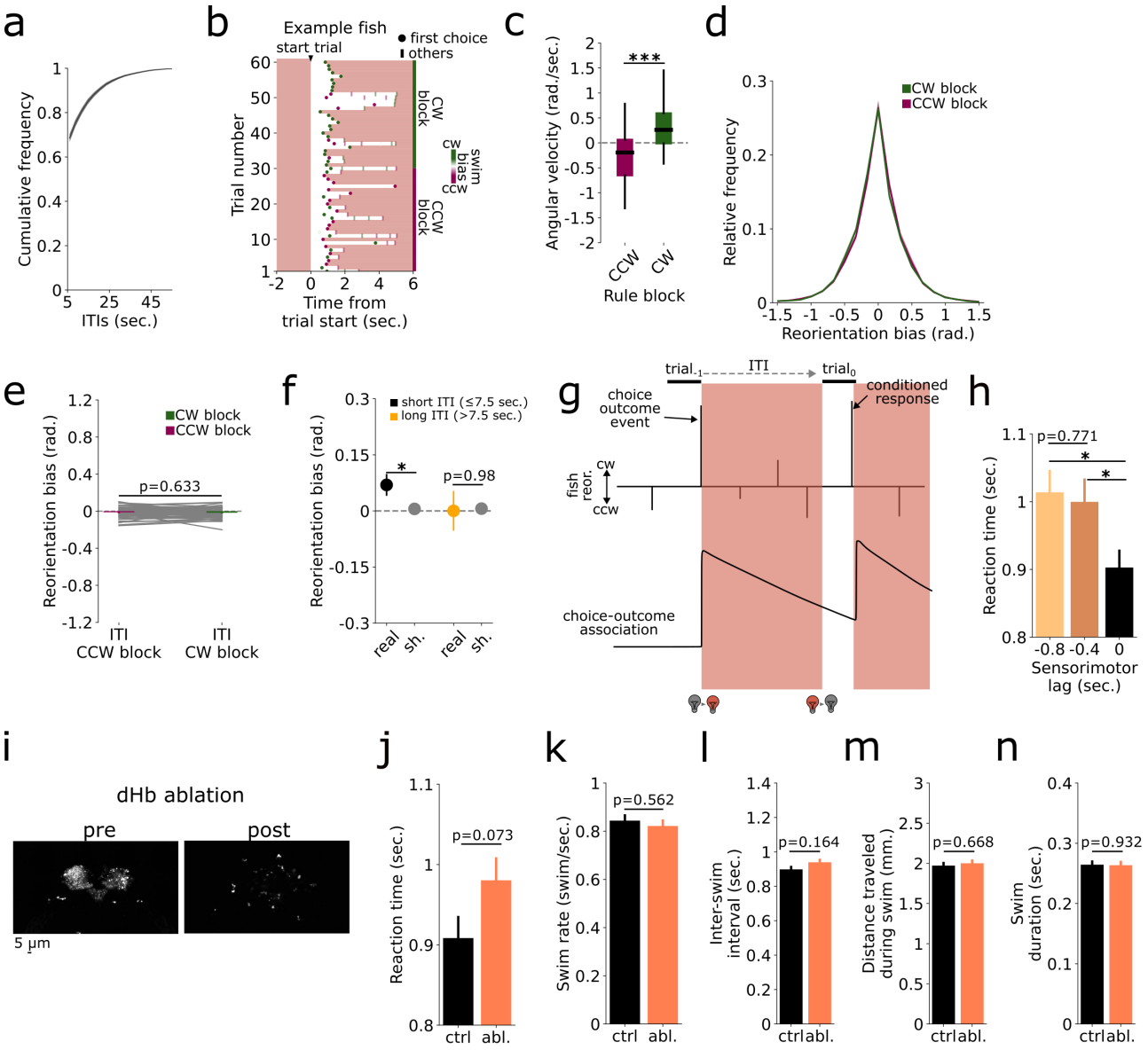

Figure S2: ***Operant thermoregulatory assay*** ***(a)*** *Cumulative distribution of ITIs during the operant assay (mean ± s.e.m.).* ***(b)*** *Example fish. Each dot represents the timing of the first choice, while bars represent subsequent choices. Color indicates turn direction (magenta: CCW, green: CW). Red sectors mark the* $temp_{UP}$ *condition.* ***(c)*** *Average angular velocity from 0.5 to 0.9 seconds after* $temp_{DOWN}$ *(magenta: CCW block, green: CW block).* ***(d)*** *Relative frequency distribution of the reorientation bias (mean ± s.e.m.) during the ITIs of CCW (magenta) and CW (green) blocks.* ***(e)*** *Average reorientation bias (mean ± s.e.m.) during the ITIs of CCW (magenta) and CW (green) blocks. Each gray line represent a single fish.* ***(f)*** *Average reorientation bias (mean ± s.e.m.) evaluated after a short (black, ≤ 7.5 seconds) or a long (yellow, > 7.5 seconds) ITI (gray: ITI shuffles).* ***(g)*** *Schematic of the hypothesized memory process taking place during the operant assay.* ***(h)*** *Reaction time (mean ± s.e.m.). Each bar represents the time between* $temp_{DOWN}$ *and the first choice (black: 0 sec. delay, dark brown: 0.4 sec. delay, light brown: 0.8 sec. delay).* ***(i)*** *Confocal image of a pre- (left) and post-dHb ablated fish (right).* ***(j)*** *Reaction time (mean ± s.e.m.). Each bar represents the time between* $temp_{DOWN}$ *and the first choice (black: treatment control group, pink: ablation group, gray: shuffles).* ***(k)*** *Average swim rate (mean ± s.e.m.) for control (black) and ablation (pink) group.* ***(l)*** *Average inter-swim interval duration (mean ± s.e.m.) for control (black) and ablation (pink) group.* ***(m)*** *Average distance traveled during a swim (mean ± s.e.m.) for control (black) and ablation (pink) group.* ***(n)*** *Average swim duration (mean ± s.e.m.) for control (black) and ablation (pink) group.*

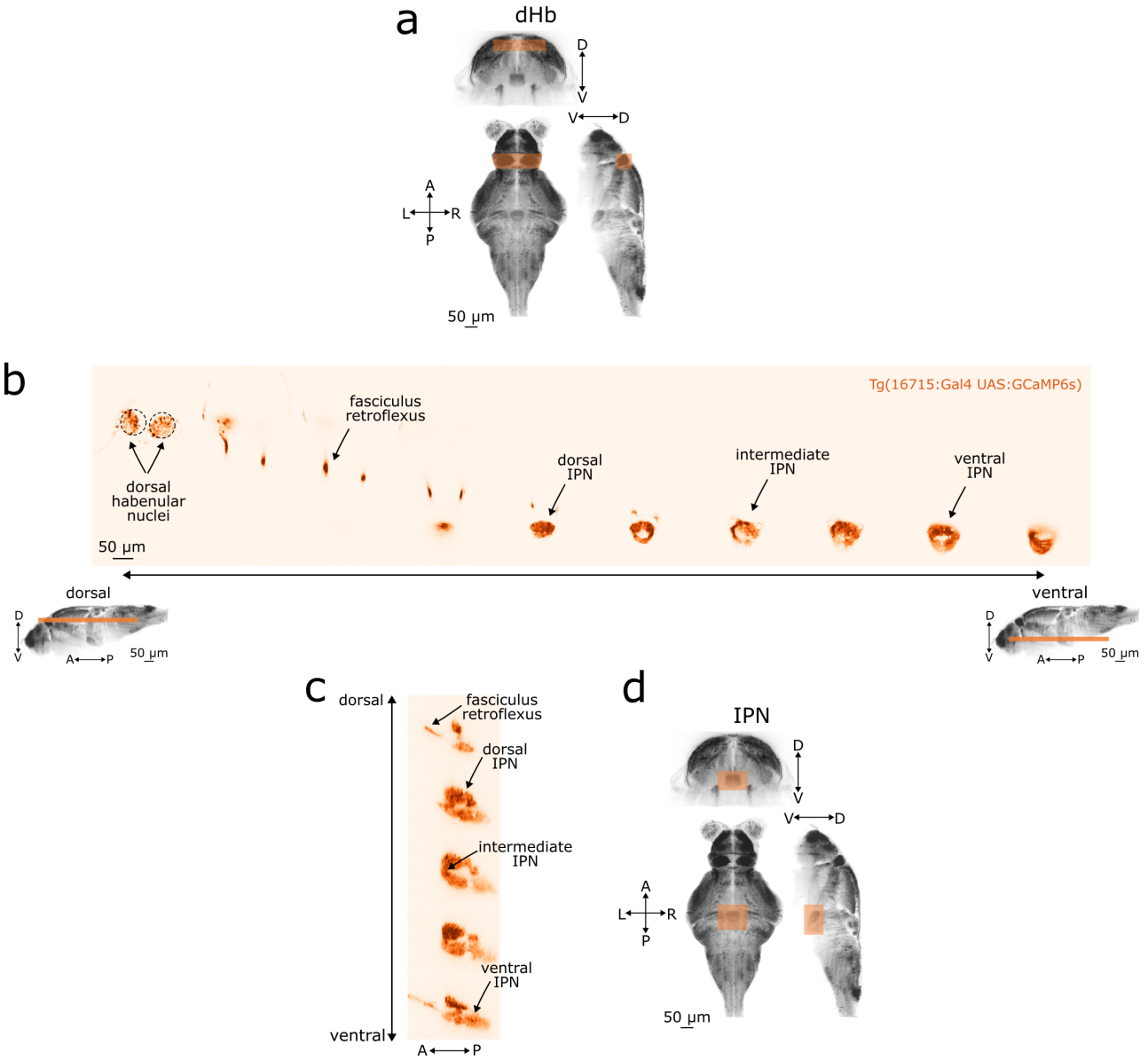

Figure S3: *dHb-IPN pathway* ***(a)*** *dHb anatomical position. Top: frontal projection. Left bottom: horizontal projection. Right bottom: sagittal projection. Reference space and anatomy from mapZebrain atlas.* ***(b)*** *Horizontal sections of dHb-to-IPN projections, labeled with the line Tg(16715:Gal4; UAS:GCaMP6s).* ***(c)*** *Sagittal sections of dHb axons in the IPN.* ***(d)*** *IPN anatomical position. Top: frontal projection. Left bottom: horizontal projection. Right bottom: sagittal projection. Reference space and anatomy from mapZebrain atlas.*

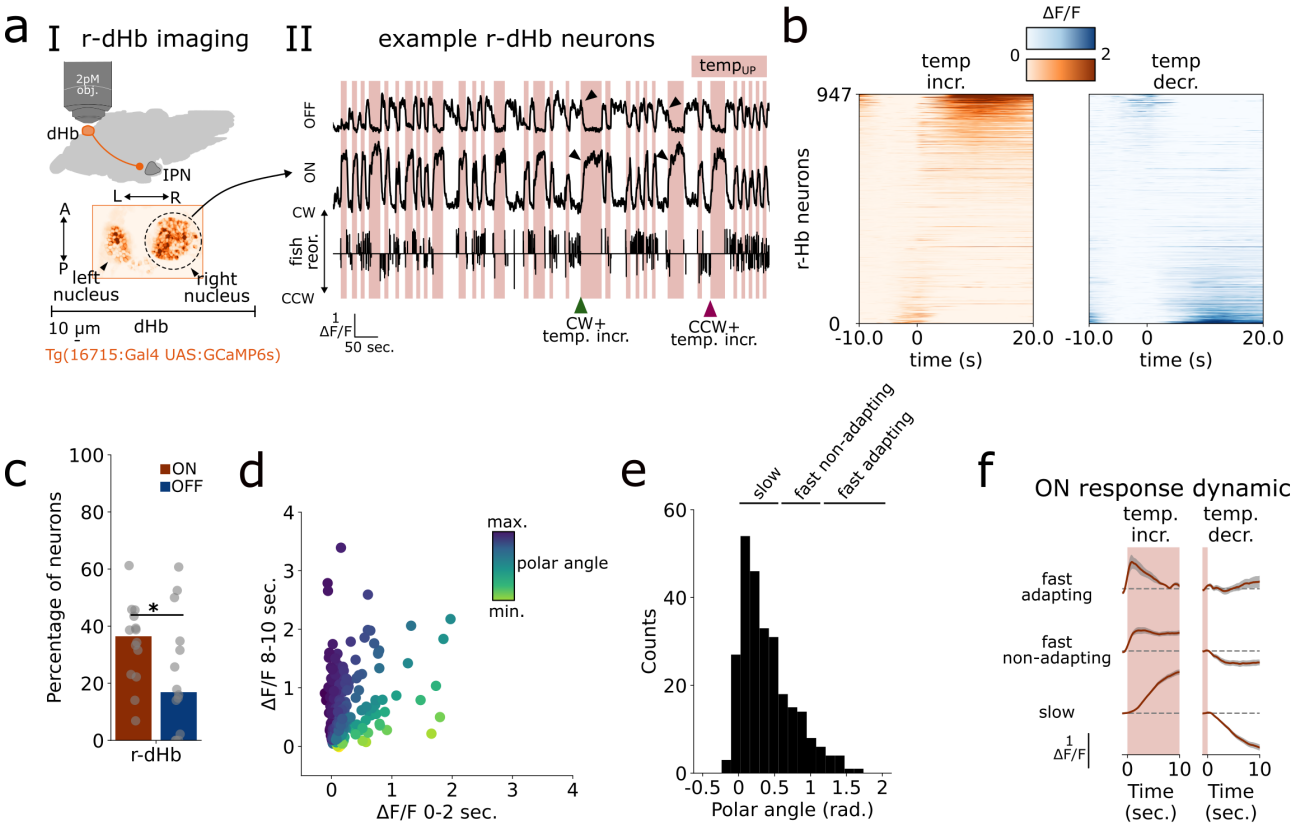

Figure S4: *dHb calcium imaging experiment* ***(a)*** *I: Top: Schematic of r-dHb 2-photon calcium imaging experiments. Bottom: Sum projection from an example recording. II: Example of OFF (top) and ON (bottom) r-dHb temperature responses. The black trace below represents the animal's behavior, with upward and downward spikes indicating CW and CCW reorientations, respectively. Green and magenta arrowheads point to CW+temp$_{UP}$ and CCW+temp$_{UP}$ events, respectively.* ***(b)*** *Triggered average at temp$_{UP}$ and temp$_{DOWN}$. Each row represents the activity of a single neuron, with correspondence between the left and the right plot. Traces have been sorted by peak activity at temp$_{UP}$.* ***(c)*** *Percentage of ON (brown) and OFF (blue) neurons in the r-dHb. Each dot represents the percentage for a single fish, with bars indicating the median.* ***(d)*** *Polar angle computation. Each dot is a neuron, color-coded by the polar angle.* ***(e)*** *Polar angle distribution of r-dHb neurons.* ***(f)*** *ON neuron response dynamics (mean ± s.e.m.). Each line shows the average activity for response types (rows) across temp$_{UP}$/temp$_{DOWN}$ events (columns).*

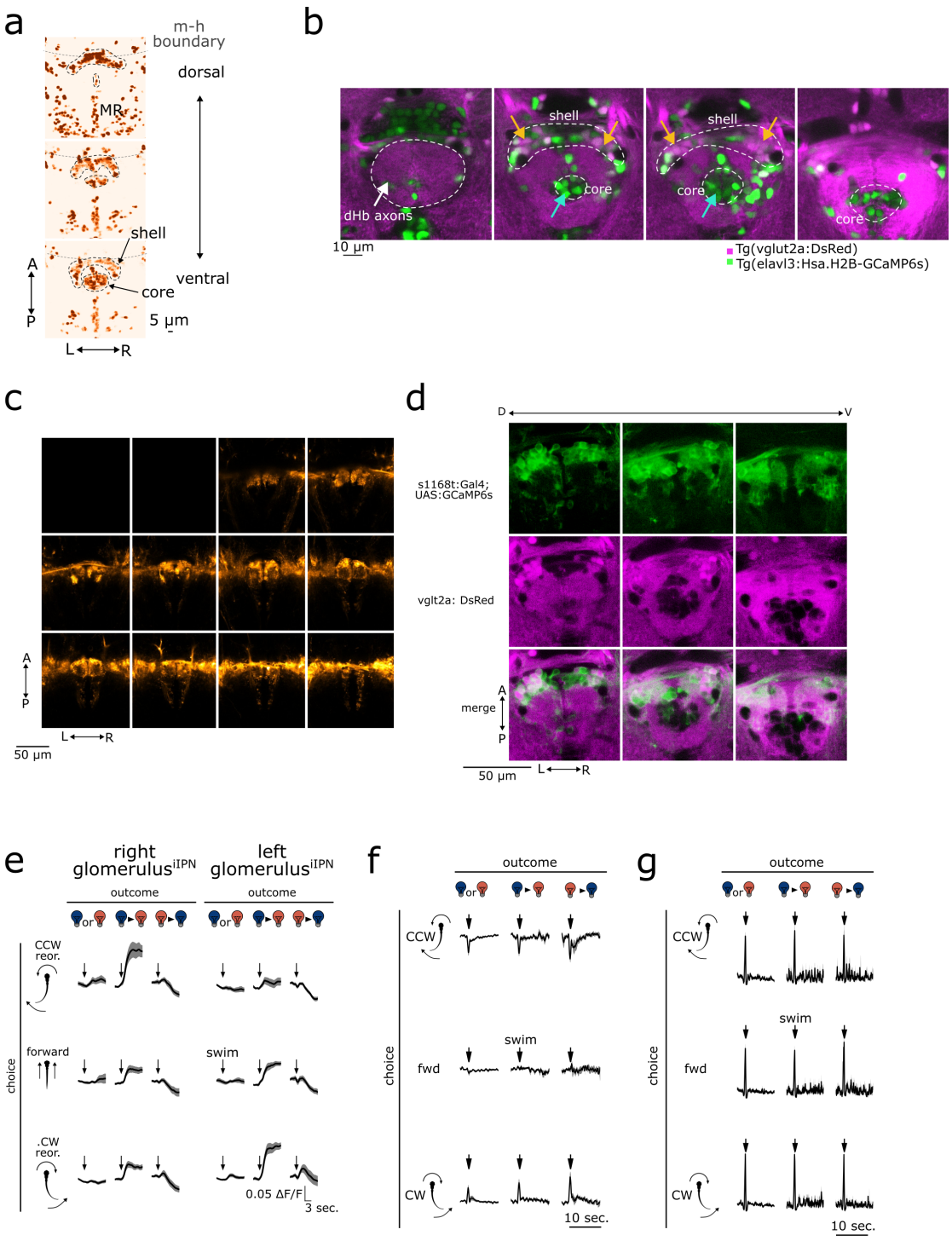

Figure S5: *Glomerulus^{iIPN} calcium imaging experiment* ***(a)*** *2-photon horizontal sections of the IPN somatic distribution in three planes. IPN shell and core and indicated by the arrows. (MR: median raphe, m-h boundaty: midbrain hindbrain boundary)* ***(b)*** *2-photon horizontal sections of Tg(vglut2a:DsRed);Tg(elavl3:Hsa.H2B-GCaMP6s), labeling in red (appearing magenta in the image) excitatory neurons and in green the nuclei of all neurons. The iIPN shell (orange arrows) contains many glutamatergic neurons, while the core (cyan arrows) does not. dHb axons are also visible, as they are also glutamatergic.* ***(c)*** *2-photon horizontal sections of the transgenic line Tg(s1168t:Gal4; UAS:GCaMP6s). Dorsoventral planes are shown from top left to bottom right.* ***(d)*** *2-photon horizontal sections of Tg(vglut2a:DsRed);Tg(s1168t:Gal4; UAS:GCaMP6s) labeling in red (appearing magenta in the image) excitatory neurons and in green the image iIPN neurons.* ***(e)*** *Triggered average (mean ± s.e.m.) for the right and left glomerulus^{iIPN} for different choice-outcome combinations.* ***(f)*** *Tail angle analysis for different choice-outcome combinations (mean ± s.e.m.). Rows represent choices, and columns represent outcomes.* ***(g)*** *Tail vigor (defined as the standard deviation over a 50 millisec. rolling window) analysis for different choice-outcome combinations (mean ± s.e.m.). Rows represent choices, and columns represent outcomes.*

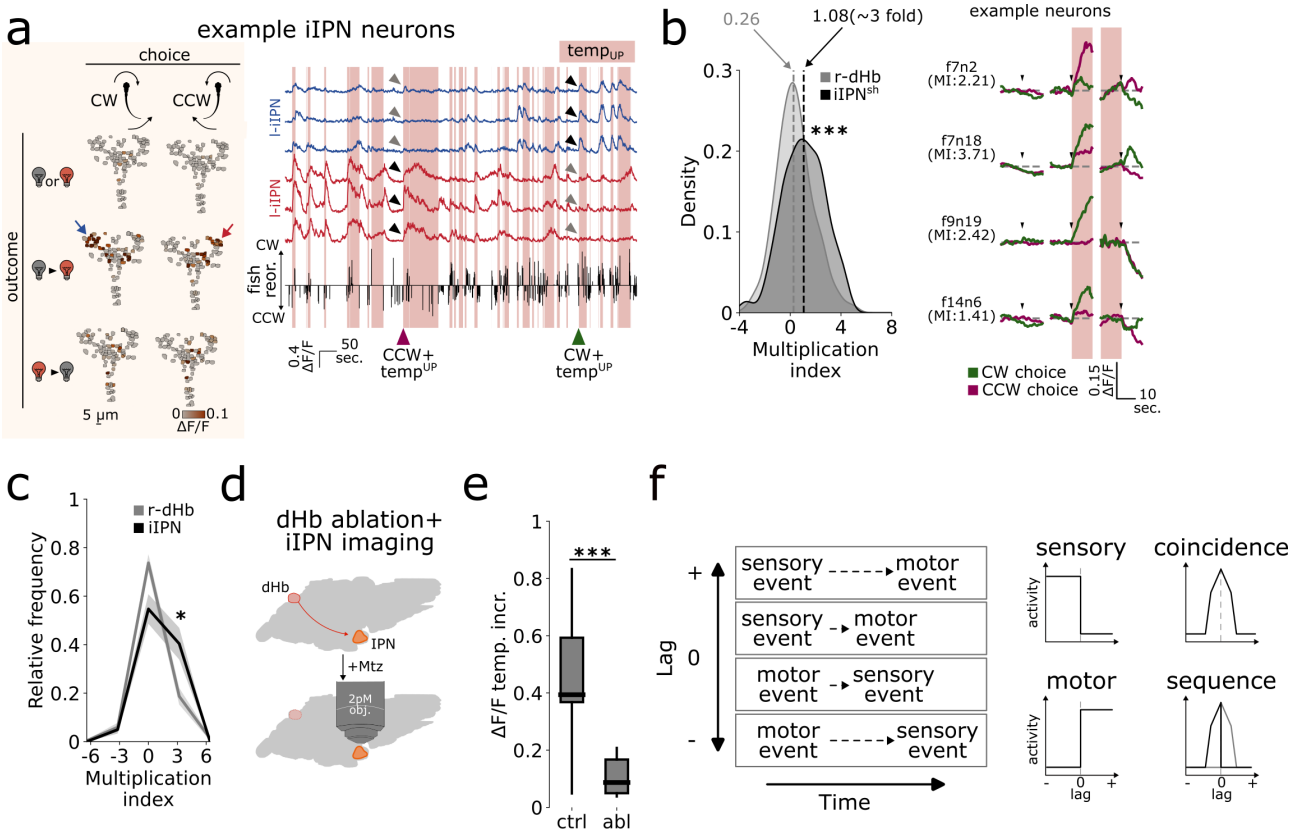

Figure S6: ***Somatic imaging of iIPN neurons and comparison with r-dHb coding*** ***(a)*** *Left: Average ΔF/F of an iIPN recording for CW and CCW choices (columns) and outcomes (rows). Right: Six example traces from the left (blue) and right (red) shell. The black trace below represents the animal's behavior, with upward and downward spikes indicating CW and CCW reorientations, respectively. Green and magenta arrowheads point to CW+temp$_{UP}$ and CCW+temp$_{UP}$ events, respectively.* ***(b)*** *Left: Multiplication index density for r-dHb (gray) and iIPN (black) neurons. Right: Example iIPN responses (rows) for no outcome (first column), temp$_{UP}$ (second column) and temp$_{DOWN}$ (third column) (magenta: CCW choice, green: CW choice). For each neuron, the fish (f) number and the neuron (n) number, as well as its multiplication index (MI), are indicated.* ***(c)*** *Average relative distribution (mean ± s.e.m.) of the multiplication index for r-dHb (gray) and iIPN (black).* ***(d)*** *Schematic of dHb ablation combined with iIPN 2-photon calcium imaging.* ***(e)*** *Average ΔF/F increase at temp$_{UP}$ for controls and ablation group.* ***(f)*** *Left: Sensorimotor lag concept. Right: Possible outcomes for the sensorimotor lag analysis.*

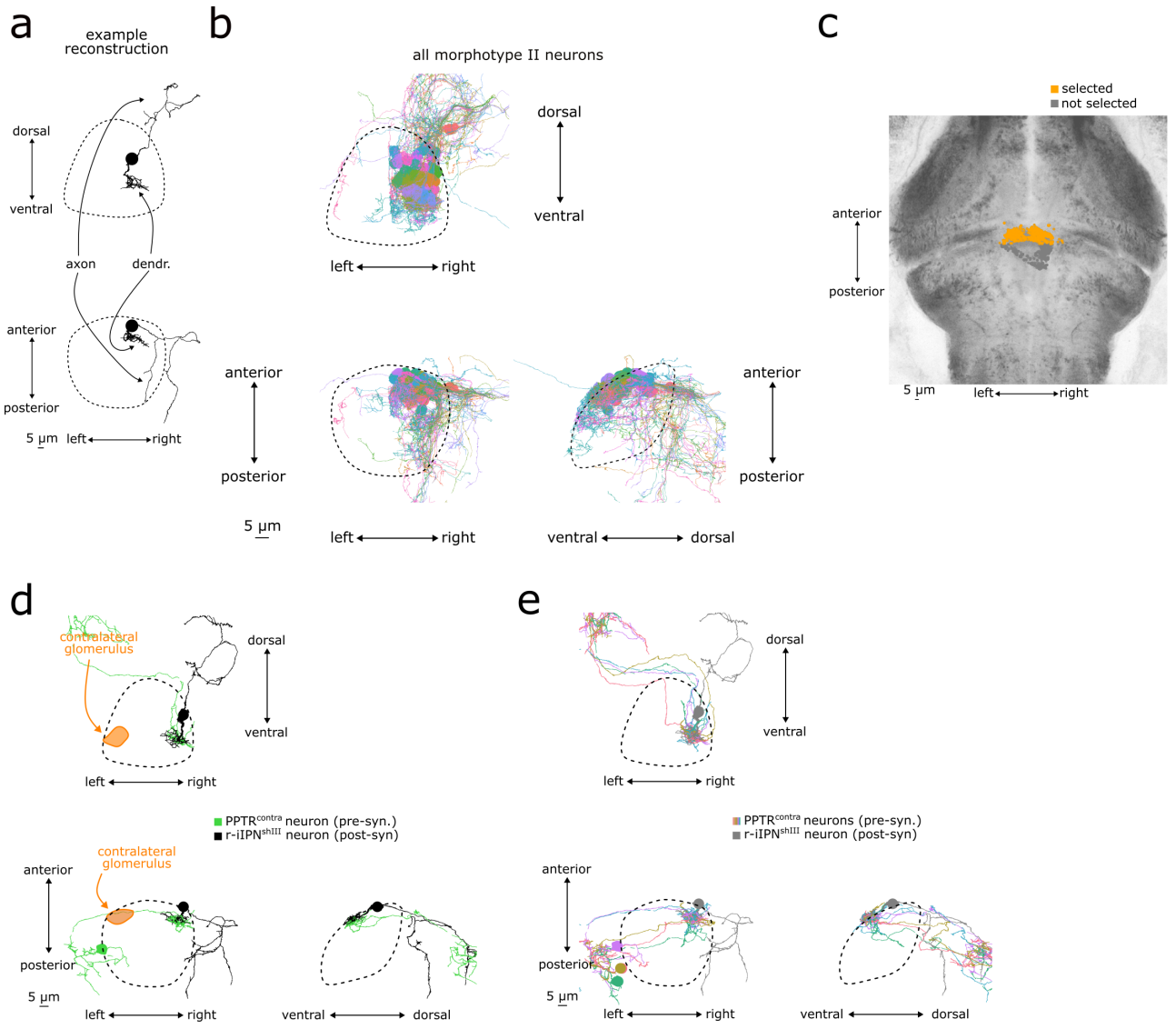

Figure S7: *EM reconstructions* ***(a)*** *Example iIPN neuron. Frontal projection on the top row and horizontal projection on the bottom row. Dashed regions enclose the IPN neuropil.* ***(b)*** *Selected iIPN neurons having the dendrite inside the IPN neuropil and projecting outside of it. Colors were randomly assigned to facilitate visualization. Top: frontal projection. Bottom left: horizontal projection. Bottom right: sagittal projection. Reference space from mapZebrain atlas.* ***c)*** *Detected contacts from dHb axons selected for the mediolateral distribution analysis (orange). Non-selected contacts are shown in gray. Horizontal section. Reference space and anatomy from mapZebrain atlas.* ***(d)*** *dPPR^{contra} axon with its iIPN postsynaptic partner. Green: dPPR^{contra} axon targeting iIPN dendrite. Black: iIPN neuron. Orange: putative region occupied by the contralateral glomerulus. Top: frontal projection. Left bottom: horizontal projection. Right bottom: sagittal projection. Reference space from mapZebrain atlas.* ***(e)*** *All reconstructed dPPR^{contra} presynaptic partners. iIPN neuron is shown in gray. Colors for dPPR^{contra} neurons were randomly assigned. Top: frontal projection. Bottom left: horizontal projection. Bottom right: sagittal projection. Reference space from mapZebrain atlas.*

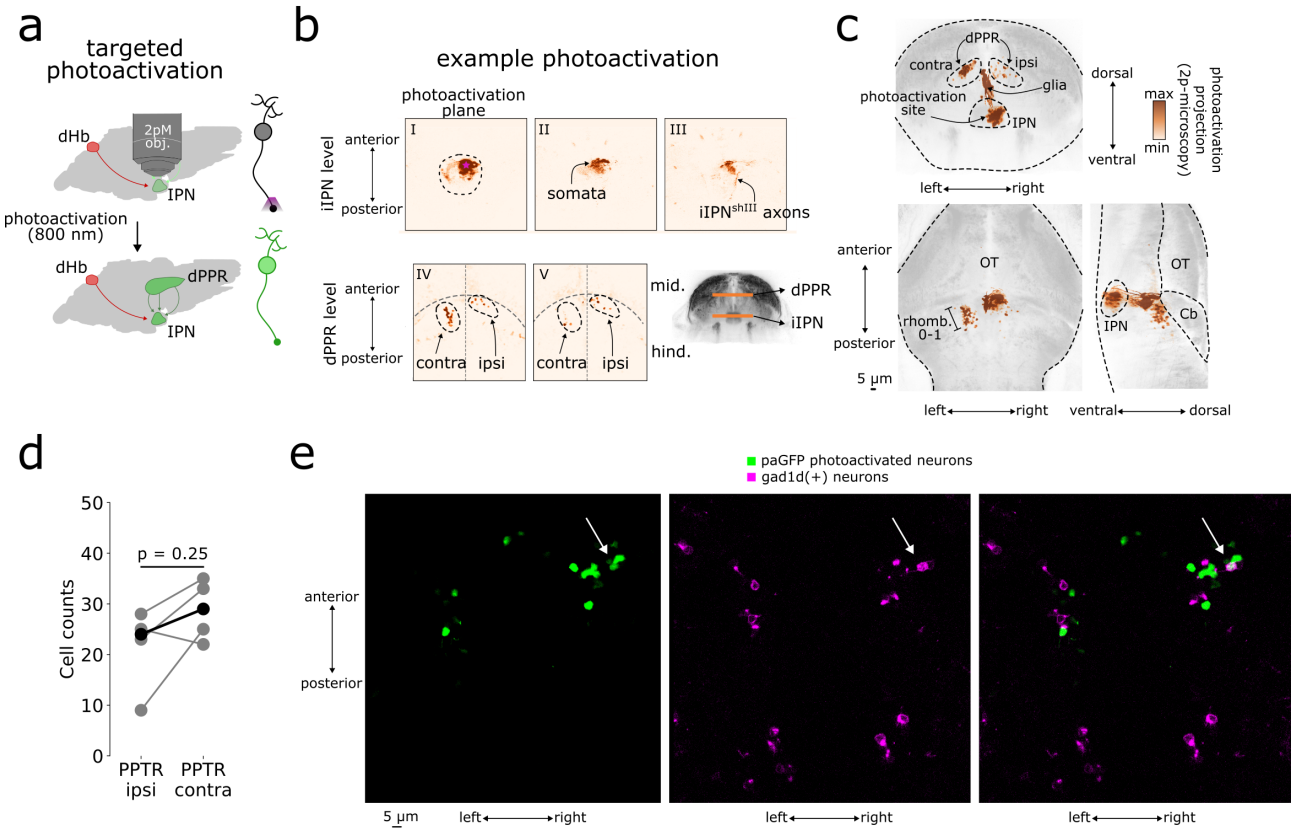

Figure S8: *Photoactivation experiments* ***(a)*** *Schematic of targeted photoactivations.* ***(b)*** *Example photoactivation. Top row: photoactivation result in the iIPN. Magenta star indicates the scanned region. dHb axons, iIPN somata, and their axons are visible. Bottom row: photoactivation result in the dPPR.* ***(c)*** *Summary map of photoactivations. The map represents the average across fish, subtracted by control acquisitions where no photoactivation was performed. Top: frontal projection. Left bottom: horizontal projection. Right bottom: sagittal projection.* ***(d)*** *Cell count of labeled dPPR neurons in the ipsilateral and contralateral hemispheres, relative to the activated side.* ***(e)*** *Co-localization of photoactivated dPPR^{ipsi} neurons and gad1b marker. Horizontal section. Green: photoactivated neurons; Magenta: inhibitory neurons gad1b(+).*

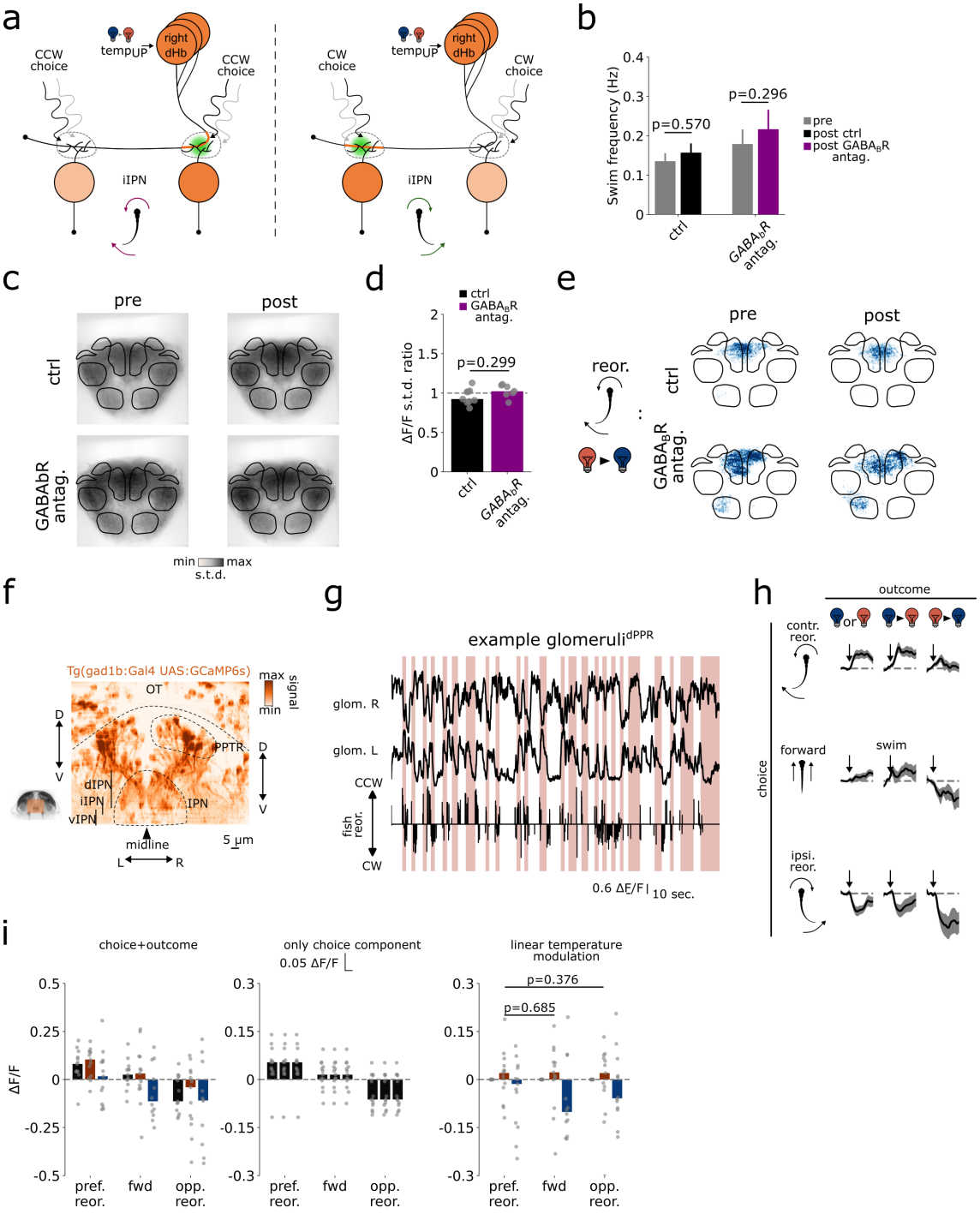

Figure S9: *iIPN inputs* ***(a)*** *Model schematic. dHb structure and function can be reconciled by modulation of axon terminals by a hypothetical neuronal population carrying choice information.* ***(b)*** *Swim frequency (number of detected swims over the 30 minutes experiment) during the first imaging session (gray bars), during the second imaging session in the ctrl group (black bar) and during the second imaging session in the treatment group (purple bar).* ***(c)*** *Average pixel-wise ΔF/F standard deviation maps. Rows represent experimental groups (first row: ctrl group, second row: treatment group) and columns represent experimental timepoint (first column: first imaging session, second column: second imaging session).* ***(d)*** *Ratio between the average pixel-wise ΔF/F standard deviation map during the first and second imaging session. If close to 1, it implies that, on average, dHb axon are similarly active during the first and second session.* ***(e)*** *Average ΔF/F projection during reorientation followed by* $temp_{DOWN}$*. Rows represent experimental groups (first row: ctrl group, second row: treatment group) and columns represent experimental timepoint (first column: first imaging session, second column: second imaging session).* ***(f)*** *Frontal projection of the line Tg(gad1b:Gal4; UAS:GCaMP6s) used during the experiment. Clear ipsilateral projections are visible.* ***(g)*** *Example recording trace from glomerulus*^{dPPR}*.* ***(h)*** *Triggered average for different choice-outcome combinations (mean ± s.e.m.).* ***(i)*** *Choice-only subraction form choice-outcome quantifications.*

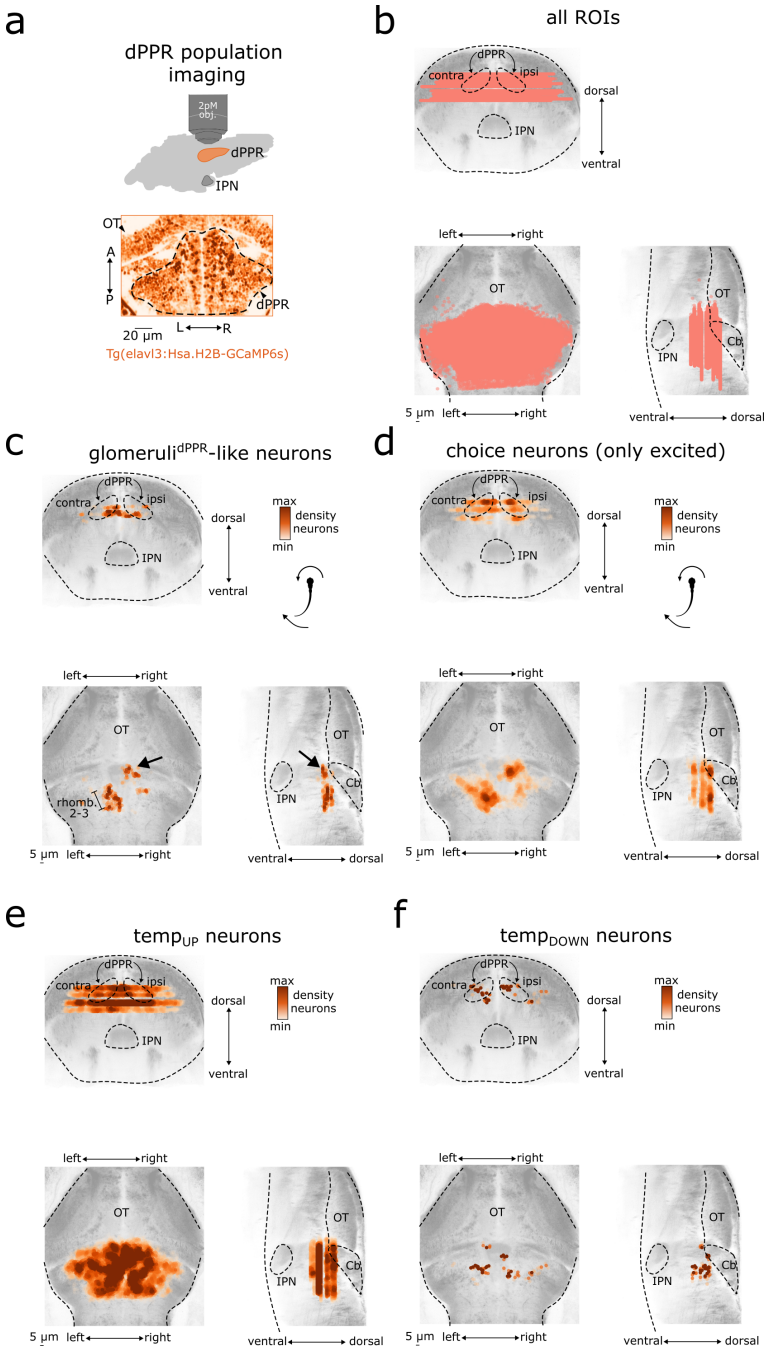

Figure S10: *dPPR somata imaging* ***(a)*** *Top: Schematic of 2-photon calcium imaging experiments in dPPR neurons. Bottom: Sum projection from an example recording.* ***(b)*** *Pooled ROIs. Top: frontal projection. Bottom left: horizontal projection. Bottom right: sagittal projection. Reference space and anatomy from mapZebrain atlas.* ***(c)*** *Density (color-coded from white to dark orange) map of bidirectional choice neurons. Top: frontal projection. Left bottom: horizontal projection. Right bottom: sagittal projection (OT: optic tectum, Cb: cerebellum). Reference space and anatomy from mapZebrain atlas.* ***(d)*** *Density (color-coded from white to dark orange) map for ROIs responding to a specific directional choice but not inhibited by the opposite. Top: frontal projection. Bottom left: horizontal projection. Bottom right: sagittal projection. Reference space and anatomy from mapZebrain atlas.* ***(e)*** *Density (color-coded from white to dark orange) map for ROIs responding to* $temp_{UP}$ *(ON neurons). Top: frontal projection. Bottom left: horizontal projection. Bottom right: sagittal projection. Reference space and anatomy from mapZebrain atlas.* ***(f)*** *Density (color-coded from white to dark orange) map for ROIs responding to* $temp_{DOWN}$ *(OFF neurons). Top: frontal projection. Bottom left: horizontal projection. Bottom right: sagittal projection. Reference space and anatomy from mapZebrain atlas.*

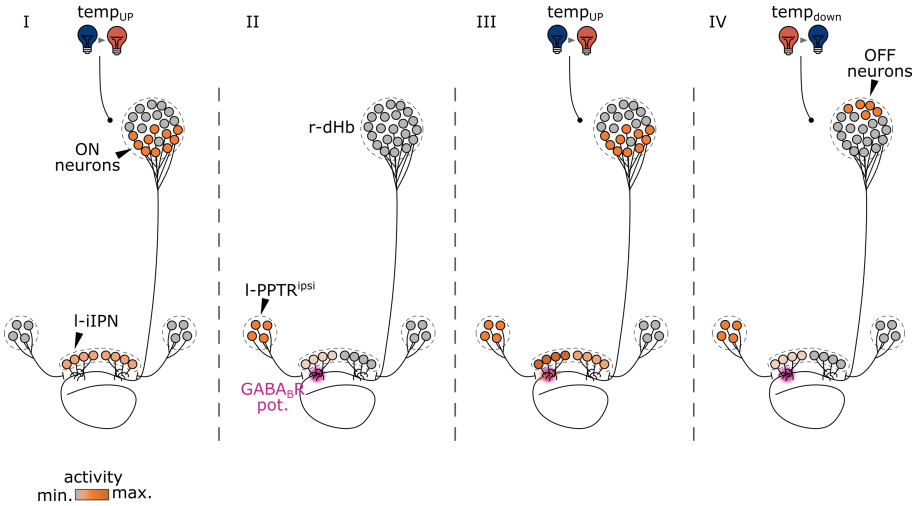

Figure S11: ***Circuit model***